Prediction of wall-pressure fluctuations for separating/reattaching flows applied to space launchers using zonal detached eddy simulation-based convolutional neural networks

Simon Lecler, Pierre-Elie Weiss, Sébastien Deck

To cite this version:

Simon Lecler, Pierre-Elie Weiss, Sébastien Deck. Prediction of wall-pressure fluctuations for separating/reattaching flows applied to space launchers using zonal detached eddy simulation-based convolutional neural networks. Physics of Fluids, 2023, 35 (6), pp.061301. 10.1063/5.0146358 . hal-04133854

HAL Id: hal-04133854
https://hal.science/hal-04133854v1

Submitted on 20 Jun 2023

Accepted to Phys. Fluids 10.1063/5.0146358

Prediction of wall pressure fluctuations for separating/reattaching flows applied to space launchers using Zonal Detached Eddy Simulation-based convolutional neural networks

S. Lecler,[1] P.E. Weiss,[1] and S. Deck[1]
DAAA, ONERA, Université Paris Saclay
F-92190 Meudon, France

(*Electronic mail: sebastien.deck@onera.fr)

(*Electronic mail: Author to whom correspondence should be addressed: pierre-elie.weiss@onera.fr.)

(*Electronic mail: simon.lecler@onera.fr.)

(Dated: 12 May 2023)

Convolutional neural networks (CNN) are used to predict the fluctuating wall-pressure coefficient and associated single-point pressure spectra in the separating/reattaching flow region around a generic space launcher configuration in the transonic regime. The neural networks are trained on a generic axisymmetric afterbody configuration. A ZDES (Zonal Detached Eddy Simulation) simulation of a semi realistic launcher geometry (NASA (National Aeronautics and Space Administration) Model 11 hammerhead) is performed and validated using available experimental results. This configuration is used as a testing case for the trained models. It is shown that the CNNs are able to identify flow features related to physical phenomena of the flow. From this feature identification, the models are able to predict the evolution of fluctuating wall quantities and locate the regions of high pressure fluctuations. A scaling procedure is proposed to retrieve correct levels of the predicted quantities for a given unknown configuration having different free stream conditions. We also demonstrate that the present models perform well applied on RANS (Reynolds-Averaged Navier-Stokes) mean flow fields, paving the way for a significant reduction in the computational cost for predicting wall-pressure fluctuations around space launchers.

Accepted to Phys. Fluids 10.1063/5.0146358

I. INTRODUCTION

Launch vehicles can experience high-level pressure fluctuations leading to unsteady aerodynamic loads during transonic flight[1–4]. These fluctuations originate from physical phenomena such as boundary layer turbulence, shock-waves oscillations, separating/reattaching flows among others. The unsteady pressure field resulting from the latter phenomenon is highly dependent on the launcher geometry and needs to be assessed for each new configuration[1]. In particular, the root-mean-square (RMS) pressure coefficient and the wall-pressure spectra in the transonic regime are highly critical quantities for the design of space launchers. They characterise the overall levels of fluctuations and allow to identify the most energetic frequencies, respectively. In addition, the induced wall-pressure fluctuations are most extreme at transonic conditions, where the launcher approaches the maximum dynamic pressure, shock waves appear and interact with other flow phenomena.

These fluctuating quantities can be obtained using unsteady scale-resolving numerical simulations. Direct numerical simulations (DNS) and Large Eddy Simulations (LES) are still impractical in engineering applications due to the high grid resolution needed for high Reynolds number wall-bounded flows[5]. The development of hybrid RANS-LES methods[6–8] which alleviates the grid resolution constraints in the near-wall regions of the flow, made the prediction of the fluctuating fields for complex launcher configurations affordable[9–12]. However, in the earlier phases of design, numerous iterations in the launcher's geometry are needed, and the previously mentioned CFD approaches are still too expensive and time-consuming to be massively used. This constraint can be overcome by using a surrogate model, namely a mathematical approximation built from high-fidelity simulation results and much faster to run. This allows to achieve a trade-off between computational time and model precision.

The most widely used models to predict wall-pressure fluctuations are either empirical correlations or analytical models[13]. The former are built from empirical databases of mean-square wall-pressure, pressure spectra or cross-spectra. A mathematical expression that fits the data is proposed. Most of these models only focus on the turbulent boundary layer. Corcos [14,15] proposed one of the first empirical models that inspired most of the subsequent models. Although it has been very popular due to its simple mathematical formulation, it is known[16] to overpredict levels of the spectrum at wavenumbers below the convective peak. Corcos formulation has been improved by several authors. For instance, Efimtsov[17] takes into account the boundary layer thickness and his model is calibrated on measurements on compressible flows over aircrafts. Ffowcs-Williams [18] and Chase [19,20] complexified Corcos formulation to describe more accurately the low wavenumber region, while Caiazzo *et al.*[21] proposed a general formulation preserving the initial mathematical simplicity. According to several authors[22,23], the empirical model that best performs on predicting the turbulent boundary layer wall-pressure spectrum is the one proposed by Goody[24]. The latter has been recently generalised to adverse-pressure gradient and various flow conditions by Catlett *et al.* [25], Rozenberg, Robert, and Moreau [26], Hu [27] and Lee [22]. Finally, Robertson [28] developed empirical correlations for axisymmetric bodies in the transonic regime, considering attached and separated flows and shock-wave oscillations. The drawback of such empirical models is their reliability and their relatively short scope, as they are built from limited data obtained from a few experimental configurations and conditions.

Conversely, analytical models are based on the derivation of a solution of the Poisson equation governing the pressure fluctuations:

$$\frac{1}{\rho}\nabla^2 p' = -2\frac{\partial u'_j}{\partial x_i}\frac{\partial U_i}{\partial x_j} - \frac{\partial^2}{\partial x_i \partial x_j}\left(u'_i u'_j - \overline{u'_i u'_j}\right) \tag{1}$$

with p' the fluctuating component of pressure, ρ the density, U_i and u'_i, $i \in [1,3]$ the mean and fluctuating velocities, respectively.

Two approaches are classically used: the first one solves the equation directly in the space-time domain, whereas the second one derives a spectral solution through the wavenumber-frequency spectrum. The former was followed by Peltier and Hambric [29] and Slama *et al.*[30]. However, the space-domain approach is challenging from the numerical point of view, since a six-dimensional integration has to be performed to compute the cross-correlation of wall-pressure fluctuations, followed by the a 3D Fourier transform to compute the wavenumber-frequency spectrum[31]. The accurate computation of these models along the entire wall of a launcher would thus require huge computational time and resources. The second approach was first proposed by Kraichnan [32], followed by Panton and Linebarger [33] and Remmler *et al.* [34]. The resolution of the Poisson equation in the spectral domain involves the modelling of the two-point statistics of the turbulent velocity. Finally, following Blake [35], some authors provided an approximate solution of the Poisson equation, calibrated for attached flows around airfoil trailing edges (see Bertagnolio *et al.*[36], Kamruzzaman *et al.* [37] and Stalnov *et al.*[38]). Finally, a very comprehensive analytical model for the prediction of the unsteady wall-pressure field was published by Grasso *et al.* [31], including adverse

Accepted to Phys. Fluids 10.1063/5.0146358

pressure gradient effects and both rapid and slow terms involved in the Poisson equation.

However, these analytical models are only valid for incompressible attached flows and have been calibrated for turbulent boundary layers and airfoil trailing edges and cannot be applied straightforwardly to complex separated flows around space launchers. These flows are characterised by the development of a shear layer that impinges the wall, leading to high-level pressure fluctuations. The reattachment zone is followed by a wake composed of vortical structures which are shed downstream (analogous to the vortex shedding phenomenon[39]).

From a different perspective and the availability of detailed databases due to the upsurge of computational power, Machine Learning (ML) has rapidly been becoming an appealing approach for scientific computing offering numerous opportunities to tackle non-laminar flow problems as those described previously. Hence in this work, we propose a data-driven approach to build a surrogate model for predicting the fluctuating wall-pressure field for such flow configurations and conditions, taking advantage of the large amount of data produced by advanced numerical simulations. Among machine learning techniques, artificial neural networks have proved to be powerful tools in the fields of computer vision[40] or natural language processing[41]. Due to their ability to learn highly nonlinear relationships between inputs and outputs, they have drawn researchers' interest in the field of fluid dynamics. They have already been used to address aerodynamic problems[42,43] such as flow control[44], improvement of RANS models[45–48], flow field reconstruction[49,50], aerodynamic response prediction[51–57]and features identification and extraction[58].

Table I gathers some recent studies that used artificial neural networks to predict flow fields and aerodynamic quantities. One can note that most of these studies aim at predicting mean flow quantities for airfoils or simple geometry shapes. However, some authors focused on predicting fluctuating quantities for attached flows or aircraft wings using DNS or experimental data. In particular, Levinski[59] used a Radial Basis Functions (RBF, a neural network with a single hidden layer using radial basis functions as activation functions) network to predict the RMS pressure and the spectra on an aircraft wing from experimental data. Ling *et al.*[60] employed a Multilayer Perceptron (MLP, a basic feedforward neural network) trained on DNS data to predict the power spectral density of pressure fluctuations at the wall from the knowledge of the same quantity at points above the wall. More recently, Dominique *et al.*[61] used a MLP to predict the dimensionless power spectral density of pressure fluctuations for a turbulent boundary layer knowing a set of boundary layer parameters.

None of these works deal with separating/reattaching flows. Moreover, acquiring experimen-

TABLE I: Studies using artificial neural networks for aerodynamics prediction

Authors	Case	R_e	Model input	Model output	Data origin
Sekar *et al.*[51]	Airfoil	$100-2500$	Airfoil geometry, angle of attack, Reynolds number	Mean flow field (pressure, velocity)	RANS
Thuerey *et al.*[52]	Airfoil	$0.5-5\times10^6$	2D velocity fields	2D pressure field	RANS
Bhatnagar *et al.*[53]	Airfoil	$0.5-3\times10^6$	Airfoil shape + free stream conditions	2D velocity and pressure fields	RANS
Jin *et al.*[49]	Cylinder	$60-1100$	Wall pressure coefficient	2D velocity field	-
Guo *et al.*[50]	Car / 2D geometry shapes	20	Geometry (signed distance function)	2D velocity field	LBM
Guastoni *et al.*[57]	Turbulent channel flow	$Re_\tau = 180-550$	Wall shear-stress/pressure fields	Velocity fluctuations field	DNS
Ling *et al.*[60]	Turbulent boundary layer	$Re_\theta = 1075-1310$	Pressure spectra above the wall	Pressure spectra	DNS
Levinski[59]	Fighter aircraft wings	12.3×10^6	Angles of attack /sideslip	Cp_{rms} Pressure spectra	Expt
Dominique *et al.*[61]	Turbulent boundary layer	$1-1.5\times10^5$	Boundary layer parameters	Pressure spectra	Expt/DNS/LES
Present	Axisymmetric separating/ reattaching flow	2.4×10^6	Mean flow field	Cp_{rms} Pressure spectra	ZDES

tal or DNS data is a time-consuming and costly process. In this study, our objective is to build models for the prediction of unsteady quantities from mean flow data that can be obtained from RANS or hybrid RANS-LES simulations. The models identify spatial features in the flow field and infer the corresponding pressure fluctuation magnitudes or pressure spectra. Initially used in computer vision[62–64], convolutional neural network (CNNs) have become increasingly popular due to their ability to capture spatial information and extract important features in the input data. As an example, Guastoni *et al.*[57] used a convolutional neural network to predict the two-dimensional velocity fluctuations field at different wall-normal locations in a channel flow using wall-shear-stress components and wall-pressure as inputs. Jagodinski *et al.*[65] showed that CNNs are capable of predicting dynamical phenomena in turbulent flows without requiring any a-priori knowledge of the underlying dynamics, proving that CNNs are powerful tools for learning nonlinear spatial correlations in turbulent flows.

for wall pressure fluctuations prediction. Levinski[59] used a Radial Basis Functions (RBF) network to predict the RMS pressure and the spectra on an aircraft wing from experimental data. Ling *et al.*[60] employed a Multilayer Perceptron (MLP) trained on Direct Numerical Simulation (DNS) data to predict the power spectral density of pressure fluctuations at the wall from the knowledge of the same quantity at points above the wall. The exploitation of this remarkable characteristics of CNNs is at the core of the present study. Two CNNs are trained on a generic axisymmetric configuration to predict the RMS pressure coefficient and the pressure spectra at the wall for separating/reattaching flows. A high-fidelity RANS-LES simulation of a semi-realistic launcher configuration has been conducted and results are compared to existing experimental data. A testing dataset is then built from this simulation. We show that the proposed models are able to identify characteristic regions of the flow (shear layer, recirculation zone, reattachment region) and infer fluctuating quantities from these informations. They accurately locate regions of high-level pressure fluctuations and identify the most energetic frequencies in the flow for an unknown configuration presenting similar flow physics. The accurate levels of fluctuations can also be retrieved from the models outputs using a scaling procedure. Sensitivity to the turbulence model used to provide the input flow field is also analysed. This work brings the perspective of predicting fluctuating wall-pressure fields without resorting to costly unsteady simulations. To the authors' best knowledge, this study is the first attempt to predict wall-pressure fluctuations on a space launcher configuration from CFD mean flow data using data-driven models.

The paper is organised as follows: in Sec. II, the training case (S3Ch generic afterbody configuration) and the testing case (NASA model 11 hammerhead launcher) are described and the simulation process of both configurations is detailed. In Sec. III, methods associated with the prediction strategy are explained, including the construction of the dataset and the design of the CNNs architectures. An analysis of the working principle of the CNNs is presenting in Sec. IV, providing physical interpretability of the results and demonstrating the ability of the present CNNs to identify mean flow characteristics in the input data using all of the input variables in the prediction process. Results related to the training and application of the models are presented in Sec. V. The main results of this study are summarised in Sec. VI together with a discussion about the limits and possible perspectives of this work.

II. TEST CASES: DESCRIPTION AND VALIDATION

Developing a data-driven model based on artificial neural networks requires a database, a specific neural network with carefully chosen parameters, and a training algorithm to optimise the trainable parameters of the network. The design of the neural network and the training process will be discussed in section III C. Here are presented the computed configurations used to provide training and testing data for the present data-driven approach. The training dataset is built from a simulation of a transonic separating/reattaching flow around a generic afterbody geometry denoted as S3Ch. The testing data used to evaluate the trained models are provided by a simulation of a generic launcher configuration denoted as NASA Model 11.

A. Training case: S3Ch generic afterbody

1. *Geometry and numerical setup*

The generic afterbody geometry consists of an axisymmetric backward facing step designed to fit the experimental S3Ch wind tunnel configuration studied by Deprés *et al.*[66] and Meliga and Reijasse[67]. It is composed of two adjacent cylinders of different diameters. The diameter of the first cylinder is $D = 100$ mm. The second cylinder has a length L and a diameter d such that $\frac{L}{D} = 1.2$ and $\frac{d}{D} = 0.4$. ZDES simulations of this case have been highly validated in numerous previous studies[68–71].

This work is focused on the transonic flow regime at a free stream Mach number $M_\infty = 0.7$. The geometry, the sizes of the computational domain and the mesh are show in Fig. 1. The Reynolds number based on the forebody diameter is $Re_D = 1.2 \times 10^6$, the boundary layer thickness at the edge of the largest cylinder is $\frac{\delta_0}{D} = 0.2$, and the free stream dynamic pressure is $q_\infty = \frac{\gamma}{2} M_\infty^2 P_\infty \approx$ 24 815 Pa. The multiblock structured mesh is composed of 12×10^6 hexahedral cells, with 240 cells in the azimuthal direction. The time step of the simulation is $\Delta t_{CFD} = 2\ \mu$s.

To compute the RMS pressure and the power spectral density (PSD) at the wall, 41 040 numerical sensors are placed on the skin of the afterbody at 170 longitudinal positions and 240 azimuthal coordinates. The acquisition time is $T_{acq} = 0.2$ s of physical time, with a sampling frequency of 250 kHz.

2. *Main features of the mean and instantaneous flow*

The salient features of the flow are displayed in Fig. 2 (see Pain *et al.*[71] for further details). To begin with, an overview of the instantaneous turbulent field of the flow is provided in Fig. 2a with the visualisation of an isosurface of the normalised Q-criterion ($\frac{QD^2}{U_\infty^2} = 50$) coloured by the dimensionless streamwise velocity component. Toroidal eddies originating from the edge are observed, that merge together and rapidly distort to become fully three-dimensional structures. The numerical schlieren plotted in a streamwise cut-off plane and at the wall evidence the wide

Accepted to Phys. Fluids 10.1063/5.0146358

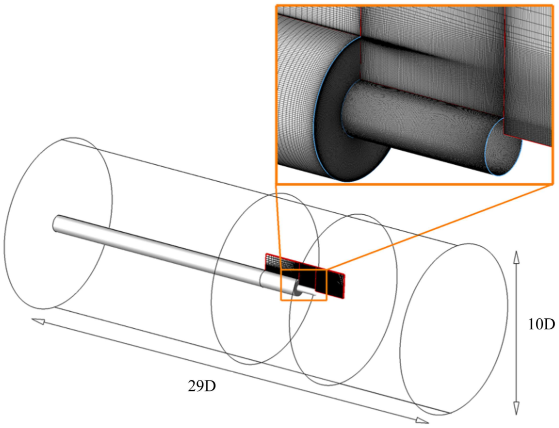

FIG. 1: Sizes of the computational domain and close-up view of the mesh in the separated zone of interest (taken from Pain *et al.* [71]).

variety of length scales in the flow. Figure 2c provides the mean organisation of the flow. The cut-off plane of the dimensionless streamwise velocity and the mean streamlines allow us to visualise the recirculation regions and the growing of the shear layer that ultimately impacts the wall. The evolution of the fluctuating wall-pressure coefficient Cp_{rms} is also plotted. A steady increase is observed, linked to the organised structures in the shear layer[72], and a plateau is reached in the reattachment region. Finally, Fig.2b displays a log-log axis plot of the normalised premultiplied power spectral density (PSD) $fG_{p'}(f)/\sigma^2$ of wall-pressure fluctuations at the position $x/D = 0.6$, with $G_{p'}$ the PSD and σ^2 the standard deviation of the fluctuating pressure. The pressure spectrum and the evolution of Cp_{rms} are in good agreement with the experimental data of Deprés *et al.*[66] and Meliga and Reijasse[67].

B. Application case: NASA model 11 hammerhead launch vehicle

1. *Geometry and numerical setup*

The basic geometry of the chosen application case is the NASA Model 11 hammerhead launch vehicle from Coe and Nute[73]. It consists of an axisymmetric launcher shape with a payload diameter larger than the second stage diameter. A separation of the flow occurs at the edge of the

Accepted to Phys. Fluids 10.1063/5.0146358

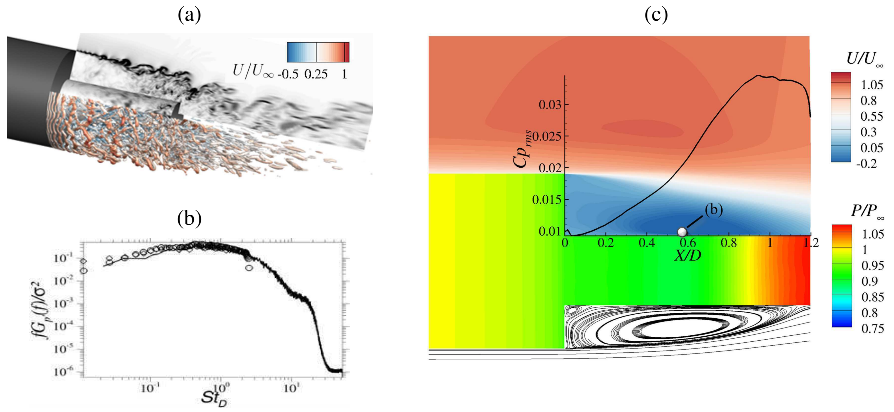

FIG. 2: (a) Isosurfaces of the normalised Q-criterion ($\frac{QD^2}{U_\infty^2} = 50$) coloured by the dimensionless streamwise velocity and numerical pseudo-schlieren (gray scale) in a cut-off plane and on the skin of the emerging cylinder (taken from Pain *et al.*[71]). (b) Normalised premultiplied PSD of the pressure at the wall for the streamwise location $x/D = 0.6$. Experimental data : (◇) Deprés *et al.*[66], (○) Meliga and Reijasse[67]. (c) RMS pressure coefficient at the wall of the emerging cylinder and mean organisation of the flow with a cut-off plane of the dimensionless streamwise velocity (top), mean streamlines (bottom) and the dimensionless static pressure at the wall.

payload due to the sudden geometrical change. A sketch of the geometry is shown in Fig. 3. The reference diameter D corresponds to the diameter at the edge of the payload fairing, just upstream of the separation point and equals 0.244 m.

This hammerhead configuration has been experimentally studied by Coe and Nute[73] and more recently by Schuster *et al.*[74], providing mean and fluctuating pressure coefficients. Coe and Nute[73] used Kulites to record pressure fluctuations at the wall. Schuster *et al.*[74] used unsteady Pressure-Sensitive Paint (uPSP), and acquired pressure signals on a larger frequency band. In this study, the free stream conditions have been selected to correspond to the wind tunnel conditions of the experiment of Schuster *et al.*[74]. The transonic Mach number is $M_\infty = 0.8$, the stagnation pressure and temperature are respectively $P_i = 236\ 255$ Pa and $T_i = 700$ K, leading to a Reynolds number based on the reference diameter $Re_D = 2.4 \times 10^6$. The angle of attack is 0°.

The computational domain and the mesh in a streamwise cut-off plane and at the wall are shown in Fig.5. The characteristic sizes of the computational domain are chosen to avoid any reflections

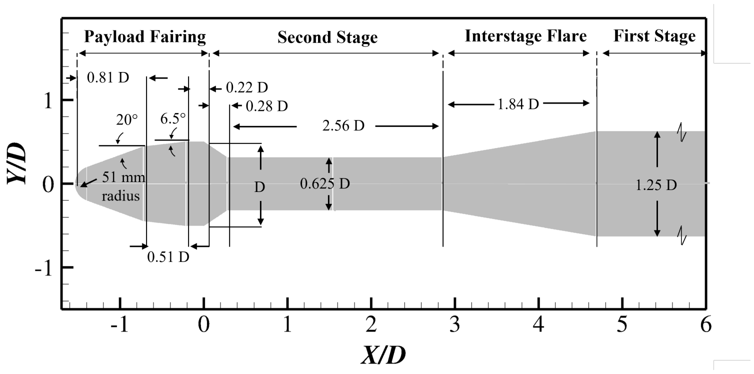

FIG. 3: Sketch of the geometry.

of spurious numerical waves. Its length and diameter are 246D and 320D, respectively. The sting holding the afterbody has been extended up to the end of the domain.

The mesh includes 24×10^6 hexahedral cells. It should be noted that the whole axisymmetric computational domain is computed in the azimuthal direction, and not only a slice of the azimuthal domain. This permits the simulation of all azimuthal modes of the flow, especially the antisymmetric mode $m = 1$ responsible for the buffets loads[68]. Besides, the domain is discretised with 240 points in this direction, as for the S3Ch generic afterbody presented in section II A 1. The grid is built using an O-H topology to avoid any singularity problem near the axis. In the wall-normal direction, the dimensionless first cell size is $\Delta y^+ = 1$ in the attached flow regions. In the LES domain, the mesh resolution complies with the recommended criteria[75]: $\Delta x \approx \delta_\omega/2$, $\Delta y \approx \delta_\omega/2$ and $\Delta z \approx \delta_\omega/20$, with $\delta_\omega = \frac{\Delta U}{max(\frac{\partial U}{\partial y})}$ the vorticity thickness of the shear layer. This is evidenced in Fig. 4, showing the evolution of $\Delta x/\delta_\omega$, $\Delta y/\delta_\omega$ and $\Delta z/\delta_\omega$ along a streamline in the shear layer. In addition, the early stages of the vorticity thickness development are modelled with 15 points, as advised by Simon *et al.*[76].

Numerical sensors are located in every cell in the streamwise direction in the separating/reattaching flow region. For each streamwise location, 4 sensors are regularly distributed in the azimuthal direction. A transient phase is required before collecting the statistics and recording the pressure time history. The simulation was run for 200 ms of physical time, corresponding to 35 flow-through times (i.e. $T = 35L/U_\infty$ with $L = 2.43$ m the length of the launcher) based on the free stream velocity. The pressure time history was recorded during 0.3 s. The time step of the simula-

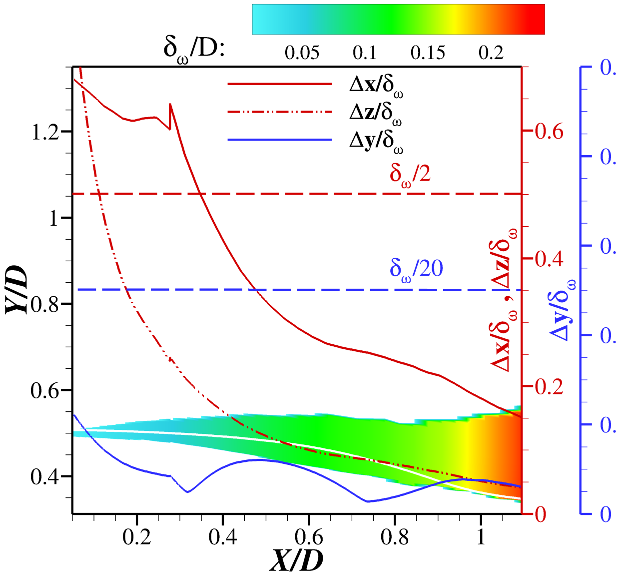

FIG. 4: Vorticity thickness δ_ω in a streamwise cut-off plane along with the evolution of $\Delta x/\delta_\omega$, $\Delta y/\delta_\omega$ and $\Delta z/\delta_\omega$ along a streamline (white line) in the shear layer.

tion equals 0.2 μs. This time step permits to obtain values of the CFL (Courant-Friedrichs-Lewy) number based on the maximum acoustic velocity $U+a$, (defined as $\frac{(U+a)\Delta t}{min(\Delta x,\Delta y,\Delta z)}$, with a the speed of sound and U the velocity magnitude) below 13 at any point of the domain. Note that the convective CFL number ($CFL = \frac{U\Delta t}{min(\Delta x,\Delta y,\Delta z)}$) is lower than 1 in the LES domain. Besides, sampling is performed every 10 time steps, corresponding to a sampling frequency of 500 kHz.

Table II compares the salient features of our simulation with the ones of other studies published in the literature. The present computation has the best temporal resolution. In addition, any modelled stress depletion issue is avoided due to the use of the ZDES approach[77].

C. Turbulence modelling with RANS and Zonal Detached Eddy Simulation (ZDES)

In this study, three computations of the NASA Model 11 configuration presented in section II B have been performed: two RANS simulations using the original Spalart-Allmaras[81] (SA) model and the Spalart-Allmaras model with Rotation Correction[82] (SA-R) as well as a high-fidelity scale resolving simulation using ZDES (Zonal Detached Eddy Simulation). The high-fidelity

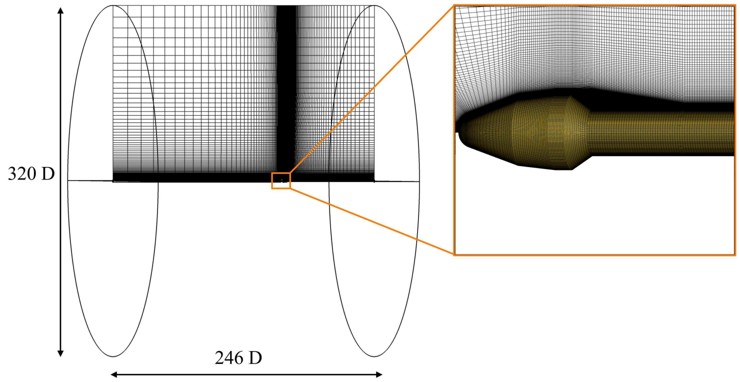

FIG. 5: Sizes of the computational domain and close-up view of the mesh in the separated zone of interest.

TABLE II: Studies performing numerical simulations of the NASA Model 11 hammerhead configuration. Re_D: Reynolds number based on the reference diameter D, $N_{xr\theta}$: total number of cells in the grid, N_θ: number of cells in the azimuthal direction, Δt_{CFD}: time step of the simulation, T_{acq}: acquisition time, f_{samp}: sampling frequency.

Authors	Re_D	$N_{xr\theta}$	N_θ	Δt_{CFD} (s)	T_{acq} (s)	$f_{samp}(kHz)$	Model
Murman and Diosady[78] (2016)	2.4×10^6	100×10^6	-	2×10^{-5}	0.5	5	DDES/SA
Murman *et al.*[79] (2017)	2.4×10^6	100×10^6	-	4×10^{-6}	5	5	DDES/SA
Liu *et al.*[12] (2019)	3.36×10^6	$6,2 \times 10^6$	100	-		19-23	DDES/SA
Wang *et al.*[80] (2021)	3.36×10^6	18.5×10^6	140	-	-	-	RSM-IDDES
Present	2.4×10^6	24×10^6	240	2×10^{-7}	0.3	500	ZDES mode 2 (2020)

computation aims at providing both input data for our models and reference output data to evaluate the models on this configuration. The RANS simulations only provide input data. In section V B, results obtained by applying our data-driven models on both ZDES and RANS mean flow fields will be compared to the reference ZDES output data (namely Cp_{rms} and wall-pressure spectra).

1. Basics of ZDES

The approach used to model the flow is the Zonal Detached Eddy Simulation (ZDES)[77,83], a hybrid RANS/LES method developed by ONERA. ZDES has been proven to be efficient in high Reynolds number configurations to simulate complex turbulent phenomena[9,10,84,85]. It aims at treating in a single model all classes of flow problems illustrated in Fig. 6. ZDES is initially based on the Spalart-Allmaras (SA) model[81]. Its formulation involves three hybrid length scales (see Eq. 2), also called modes, adapted to the three typical flow field topologies displayed in Fig. 6. The distance to the wall d_w in the SA model is replaced by $\tilde{d}_{ZDES}$:

$$\tilde{d}_{ZDES} = \tilde{d}_{mode}\left(\tilde{\Delta}, d_w, U_{i,j}, \nu, \tilde{\nu}, \frac{\partial \tilde{\nu}}{\partial n}, \frac{\partial ||\omega||}{\partial n}\right) \tag{2}$$

with $mode$ = 1,2,3, $\tilde{\Delta}$ the subgrid length scale, d_w the distance to the wall, $||\omega||$ the magnitude of vorticity, ν and $\tilde{\nu}$ the kinematic and pseudo eddy viscosity and $\frac{\partial \cdot}{\partial n}$ the derivative in the wall-normal direction. This paper is mainly concerned by mode 2 of ZDES which can be considered as the "automatic" mode of ZDES.

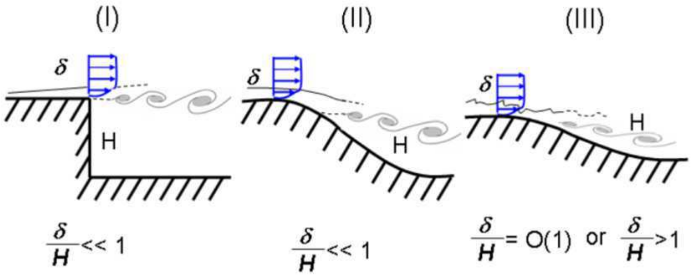

FIG. 6: Classification of typical flow problems. I: separation fixed by the geometry, II: pressure gradient induced separation on a curved surface, III: wall-modelled LES, when the separation is strongly influenced by the dynamics of the incoming boundary layer. Adapted from Deck[83].

The simulation of the NASA Model 11 configuration was made using ZDES mode 2 (2020)[77], where the switch between RANS and LES resolution is set automatically by the model itself. ZDES mode 2 (2020) is currently the only published RANS/LES formulation that provides a successful RANS shielding of attached boundary layers on arbitrarily refined grids. It should be reminded that ZDES mode 2 (2020) is, to the authors' best knowledge, the only method published in the open literature which solves the issue of possible Modelled Stress Depletion (MSD) on arbitrarily refined meshes, thus preventing any possible Grid Induced Separation (GIS).

The in-house research solver FLU3M[86] developed at ONERA was used to compute the flow. This code solves the Navier-Stokes equations on structured multiblock grids and is second-order accurate both in time and space. The RANS simulations presented in this paper were conducted using a Roe scheme with the Harten correction and a minmod limiter. This combination was chosen to ensure a good convergence of the computations. The ZDES simulation was performed using a modified low-dissipation AUSM+(P) scheme[87,88] for the convective fluxes. A MUSCL reconstruction method is used without limiter to increase the spatial accuracy of this scheme. The gradients for the diffusion fluxes are computed using the Green-Gauss method. Finally, the time discretisation is done using the implicit and second-order accurate Gear scheme with a Newton-type iterative algorithm (see Pechier, Guillen, and Cayzac [89] and Deck *et al.* [90] for further details on the numerical implementation of turbulence models).

2. *Salient features of the reference ZDES computation*

The results of the ZDES computation of the NASA Model 11 configuration are presented in this section. The objective of this computation is not to describe and analyse in deep details the physics of the flow, but to provide input mean flow data and reference output data to the proposed models. As a consequence, only the most salient mean and unsteady characteristics of the flow are presented in this section.

The acoustic CFL is defined as $\frac{(u+a)\Delta t}{min(\Delta x,\Delta y,\Delta z)}$, with a the local speed of sound. The high levels of eddy viscosity along the payload fairing evidence that the attached boundary layer is treated in URANS mode, while downstream of the separation point the ZDES switched in LES mode, as shown by the lower eddy viscosity levels. The field of acoustic CFL ensures that the time-step was carefully chosen such that this number is not greater than 13 at any point of the domain. The highest values are obtained in the attached turbulent boundary layer. Note that the conventional convective CFL number ($CFL = \frac{u\Delta t}{min(\Delta x,\Delta y,\Delta z)}$) is lower than 1 in the LES domain.

As a first glimpse of the global dynamics of the flow, Fig. 7 provides the visualisation of numerical schlieren in a streamwise cut-off plane and an isosurface of the normalised Q-criterion ($QD^2/U_\infty^2 = 0.5$). Just after the separation, toroidal structures related to the Kelvin-Helmholtz instability process are observed. They grow by pairing and are quickly replaced by three-dimensional eddies that are convected downstream[12,68]. The unsteady solution is averaged in time on the fly during the simulation.

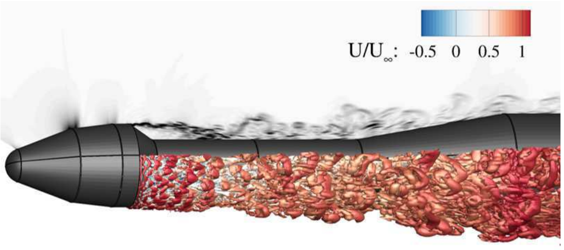

FIG. 7: Instantaneous schlieren-type visualisation in a longitudinal section (top) and isosurface of the normalised Q-criterion ($\frac{QD^2}{U_\infty^2} = 0.5$) coloured by the dimensionless streamwise velocity.

The mean flow topology is characterised by a free shear layer developing from the upstream boundary layer and impinging the wall downstream, as illustrated in Fig. 8. The mean streamlines evidence the recirculation region between separation and the mean reattachment point. The computation predicts a mean reattachment point located at $X/D = 0.94$. Schuster *et al.*[74] observed using uPSP that reattachment occurred between $X/D = 0.76$ and $X/D = 1.26$, corresponding to a mean reattachment at $X/D = 1.01$. Note also that the boundary layer thickness at the edge of the payload fairing is $\delta_0 = 0.015D$, which is significantly thinner than the boundary layer thickness of the S3Ch test case ($\delta_0/D|_{S3Ch} = 0.2$).

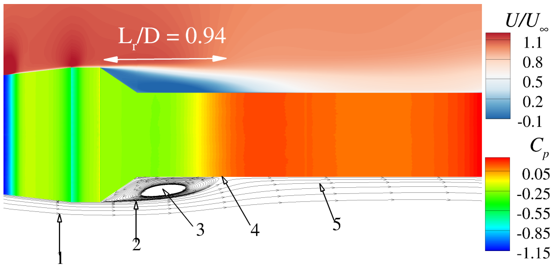

FIG. 8: Mean flow organisation : normalised streamwise velocity (top), mean streamlines (bottom) and static pressure coefficient at the wall: (1) incoming attached boundary layer, (2) shear layer, (3) recirculation zone, (4) mean reattachment point and (5) reattached boundary layer

The two fluctuating quantities of interest (*i.e.* the fluctuating wall-pressure coefficient Cp_{rms}

and the dimensionless PSD $\frac{U_\infty G_{p'}(f)}{D q_\infty^2}$) are plotted in Fig. 9 in the separating/reattaching flow region. As classically encountered in such kind of axisymmetric backward facing step flows[68,91,92], the highest levels of fluctuations are reached in the reattachment region where the mixing layer impinges the wall. The spectrum displays a broadband aspect due to the multiscale dynamics ranging from large-scale dynamics of the separated area to the fine scale eddies populating the mixing layer impinging the wall.

different in terms of diameter, Reynolds number and geometry to evaluate the generalization capability of our models and have a glimpse on the potential real-world applications.

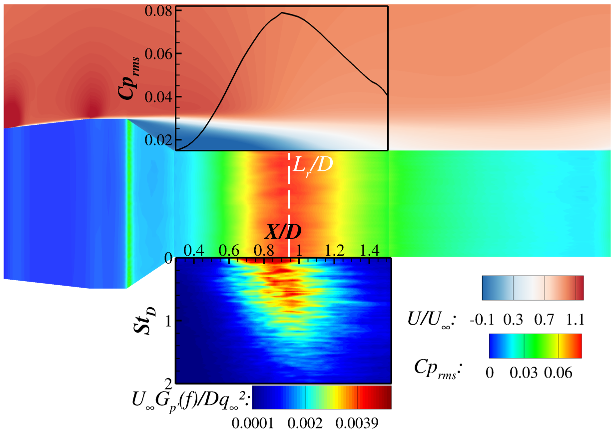

FIG. 9: Visualisation of the fluctuating quantities of interest: RMS pressure coefficient (top) and spectral map of the dimensionless power spectral density $U_\infty G_{p'}(f)/q_\infty^2 D$ (bottom) in the domain of interest defined by the interval $X/D = [0.37, 1.42]$, along with a cut-off plane of the dimensionless mean streamwise velocity and Cp_{rms} at the wall. $St_D = fD/U_\infty$ denotes the Strouhal number based on the payload diameter D. The reattachment location normalised by the reference diameter L_r/D is highlighted by a white dotted line.

The numerical results are further compared to the experimental measurements in Figs. 10, 11 and 12. The predicted mean pressure coefficient plotted in Fig. 10 is in excellent agreement with both experiments in the whole domain of study. The deviation is under 10% with respect to the Kulites measurements of Coe and Nute[73] everywhere except a small shift in the range $X/D \in [0.8-1]$. Fig.11 displays the evolution of the RMS pressure coefficient along the wall. To compare with the experimental data, the pressure spectra have been integrated in the same frequency range as in both experiments of Coe and Nute[73] and Schuster *et al.*[74]. The pressure fluctuation levels in the zone treated with URANS (before separation) are underestimated, as could be expected. In addition, compared to the Kulite measurements of Coe and Nute[73], significant deviations are observed around the expansion corner ($X/D = 4.8$). This suggests that some phenomenon such as the local oscillation of a shock-wave is not well captured in the calculation. A local refinement of the mesh near $X/D = 4.8$ could possibly improve the results as the region of interest is mostly focused in the area $X/D \leq 2$. However, the numerical results agree well with both experiments in the region of high pressure fluctuations where turbulence is resolved. In the separating/reattaching flow region, the error between the ZDES data and the measurements of Schuster *et al.*[74] is less than 10%. In addition, the computed levels of rms pressure fluctuations in the reattachment region compare well to the ones observed in similar configurations such as axisymmetric backward facing step flows or boat-tail separated flows[66,93–95].

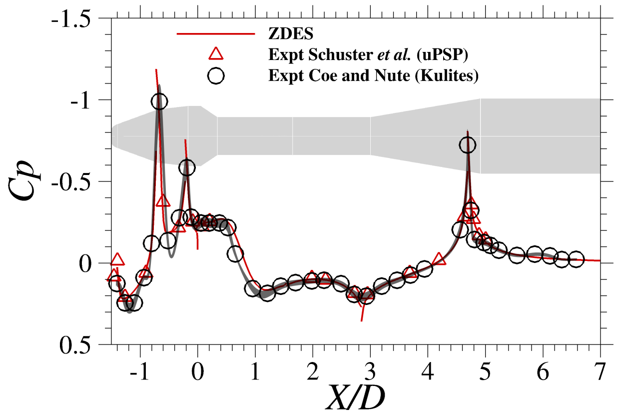

FIG. 10: Comparison of measured and computed Cp values. The grey area represents 10% difference with respect to the Kulites measurements of Coe and Nute[73].

Finally, iso-contours of filtered Cp_{rms} at the wall and two snapshots of instantaneous C_p fluctuations displayed at a 4 ms interval are shown in figures 12 b, g and f. The corresponding experimental snapshots are plotted in figures 12 a, c and e. The instantaneous visualisations of the mean pressure coefficient computed with ZDES feature similar patterns with turbulent structures of equivalent size compared with the experimental snapshots. One can note that the Cp_{rms} magni-

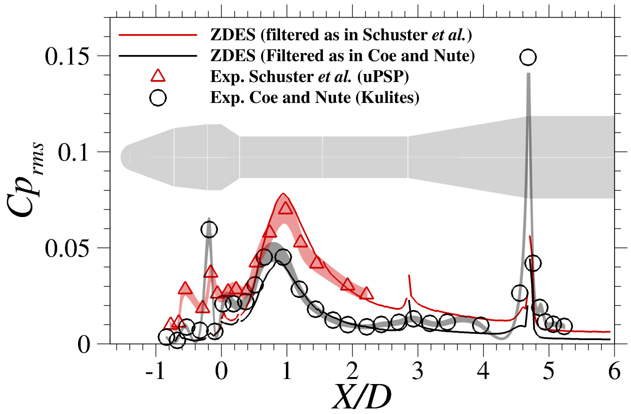

FIG. 11: Comparison of measured and computed filtered Cp_{rms} values. The values are obtained by integrating the power spectral density of pressure in the band-pass range of 10-800 Hz (i.e. $5.8 \times 10^{-3} \leq St_D \leq 0.46$) as in the experiment of Coe and Nute[73] (black) and 0-10 kHz (i.e. $0 \leq St_D \leq 5.8$) corresponding to the experiment of Schuster *et al.*[74] (red). The grey and red areas represent 10% difference with respect to the measurements of Coe and Nute[73] and Schuster *et al.*[74], respectively.

tude is slightly overpredicted by the simulation in the reattachment region (by nearly 10%), which is consistent with the plot of figure 11.

3. *Salient features of the RANS computations*

The main characteristics of the mean flow fields provided by the two RANS computations are presented in this section. The mean organisation of the flow obtained using the SA and SA-R turbulence models is shown in Fig. 13. The computed lengths of the recirculation zone L_r are also reported. Both RANS computations predict a larger recirculation bubble compared to the experiment of Schuster *et al.*[74] ($L_r/D|_{exp} = 1.01$) and to the ZDES computation ($(\Delta L_r/D)_{SA/exp} =$ 4% and $(\Delta L_r/D)_{SAR/exp} = 16\%$) while $(\Delta L_r/D)_{ZDES/exp} = 7\%$)). A similar behaviour is often observed for axisymmetric base flows (*e.g.* Simon *et al.*[97], where the SA model predicts a smaller recirculation by 6% compared to the one predicted with the SAR correction).

The mean pressure coefficients predicted by the two RANS simulations are compared to ex-

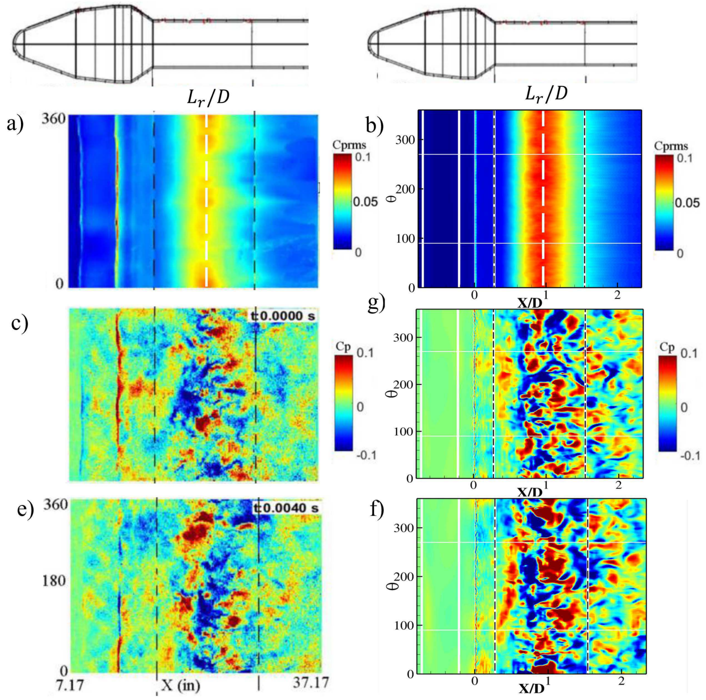

FIG. 12: Comparison between iso-contours of wall-pressure fluctuations from experimental measurements reported by Panda *et al.*[96] (a) and computed with ZDES (b). Iso-contours of the instantaneous mean pressure coefficient along the wall measured at 4 ms interval (c), (d) and equivalent snapshots from the present ZDES computation (f),(g). The reattachment location normalised by the reference diameter L_r/D is highlighted by a white dotted line.

perimental data in Fig. 14, where a very good agreement is observed, with deviations with respect the experimental data of Coe and Nute[73] less than 10% in the whole domain except in the reattachment region ($X/D \in [0.8-1.1]$), due to the difference in the predicted reattachment lengths. Indeed, as observed in Fig. 13, the turbulence model influences the size of the recirculation of the separated flow region, and consequently the evolution of the mean pressure coefficient.

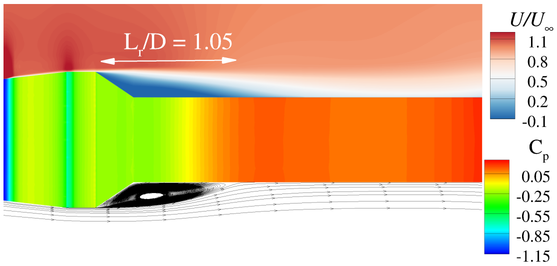

(a) RANS SA

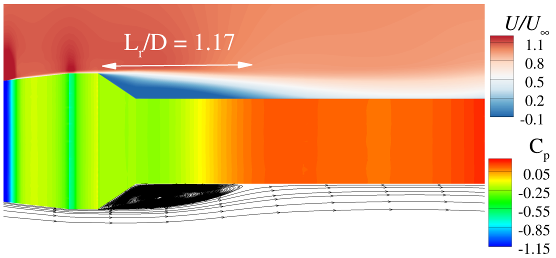

(b) RANS SA-R

FIG. 13: Mean organisation of the flow provided by RANS SA (a) and RANS SA-R (b) computations with dimensionless streamwise velocity (top), mean streamlines (bottom) and static pressure coefficient at the wall.

III. CNN BASED PREDICTION: METHODOLOGY

In this section, the CNN based methodology employed to predict the fluctuating pressure coefficient and the spectra from the mean flow field is detailed. First, the overall approach is presented. Then, the dataset construction process is described. Finally, the CNN architecture as well as the hyperparameters for training are given.

A. Overview of the prediction strategy

This work aims to reconstruct the fluctuating wall-pressure coefficient Cp_{rms} and the associated dimensionless pressure spectrum $10log_{10}\left[\frac{U_\infty G_{p'}}{Dq_\infty^2}\right](St_D)$ in a separating/reattaching flow region from mean flow data, where $St_D = fD/U_\infty$ denotes the Strouhal number based on the payload

Accepted to Phys. Fluids 10.1063/5.0146358

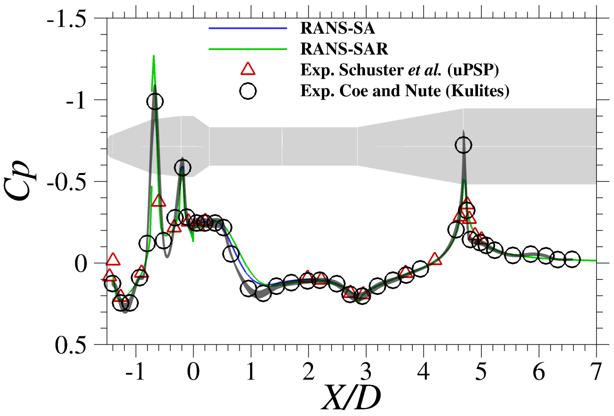

FIG. 14: Comparison of measured and computed Cp values with RANS simulations. The grey area represents 10% difference with respect to the Kulites measurements of Coe and Nute[73].

diameter D. For a given streamwise location x/D, the two prediction processes f_1 and f_2 can be described mathematically by the following mappings:

$$f_1 : \Pi(x/D) \longmapsto Cp_{rms} \tag{3}$$

$$f_2 : \Pi(x/D) \longmapsto 10log_{10}\left[\frac{U_\infty G_{p'}}{Dq_\infty^2}\right](St_{D1},...,St_{DN}) \tag{4}$$

where Π denotes the input matrix whose columns correspond to the mean flow profiles of the chosen input variables (see section III B 1) and $St_{D1},...,St_{DN}$ denote the Strouhal numbers for which the CNN outputs the corresponding PSD (see section III B 2).

The overall schematic of the prediction process is shown in Fig. 15. A preliminary CFD computation gives the mean flow field used to build the input dataset from mean flow profiles (step I). A data preprocessing step (step II) consists in standardising input and output attributes to have 0 mean and unit standard deviation. Standardising the data causes each input feature to contribute approximately equally to the training[98]. This results also in a faster convergence of the network and has been proven to yield better results in terms of mean squared errors (MSEs)[99]. The same operation is applied to the training output data. The Python library scikit-learn[100] is used to perform this standardisation. Two CNNs, referred to as CNN1 and CNN2, are developed to approximate the mapping functions f_1 and f_2, respectively (step III). Both are implemented using Tensorflow[101] with Keras API[102], that are widely used in the deep learning community. Finally, output data are rescaled back to physical units by applying the inverse standardisation operation (step IV), providing the predicted fluctuating pressure coefficient and wall-pressure spectra.

have 0 mean and unit standard deviation. This is a required practice to improve the training process and that has proven to yield better results in terms of mean squared errors (MSEs)[99]. The same operation is applied to the output training data, provided by the ZDES computation. Python library scikit-learn[100] is employed during this data preprocessing step.

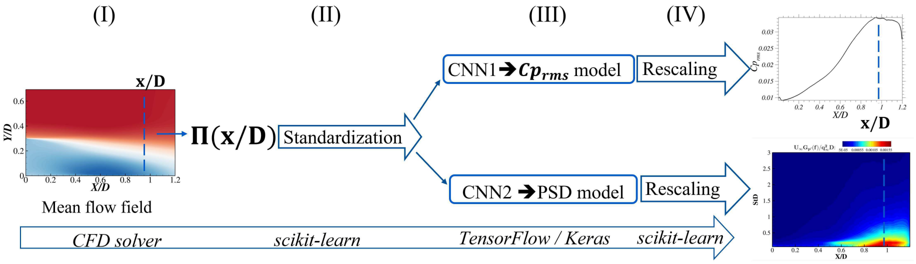

FIG. 15: Schematic diagram of the prediction process. CNN1 and CNN2 denote the convolutional neural networks that predict Cp_{rms} and the PSD, respectively.

B. CFD datasets

The CFD computations presented in section II are used to provide training and testing data. The training set is built from mean flow profiles, Cp_{rms} at the wall and corresponding pressure spectra provided by the ZDES computation of the S3Ch configuration (see section II A). Testing data are collected from ZDES and RANS computations of the NASA Model 11 configuration. Both studied geometries being axisymmetric, the mean flow variables are averaged along the azimuthal direction.

1. Input datasets

For a given streamwise position along the wall, the input matrix consists of the concatenated wall-normal flow profiles of 8 normalised input variables reported in Table III. The choice of these mean flow variables is based on a literature review of the most advanced analytical models[31,36,103] used to predict wall-pressure fluctuations from mean flow data by approximating the solution of the Poisson equation that governs pressure fluctuations. These analytical models perform the mappings of Eqns. (3) and (4) for boundary layer attached flows. Thus, this study aims to use CNNs instead of analytical expressions to predict wall-pressure from similar input data. The studied flows being compressible, conservative variables ρU and ρV are considered instead of U and V, with ρ the density, U and V the mean streamwise and wall-normal velocity components, respectively.

TABLE III: Flow variables used as input for the neural networks.

Input	Raw input	Normalisation factor
Streamwise velocity	ρU	$\rho_\infty U_\infty$
Wall-normal velocity	ρV	$\rho_\infty U_\infty$
Streamwise velocity gradient along the streamwise direction	$\frac{\partial \rho U}{\partial x}$	$\frac{\rho_\infty U_\infty}{D}$
Normal velocity gradient along the streamwise direction	$\frac{\partial \rho V}{\partial x}$	$\frac{\rho_\infty U_\infty}{D}$
Streamwise velocity gradient along the normal direction	$\frac{\partial \rho U}{\partial y}$	$\frac{\rho_\infty U_\infty}{D}$
Normal velocity gradient along the normal direction	$\frac{\partial \rho V}{\partial y}$	$\frac{\rho_\infty U_\infty}{D}$
Static pressure	P	q_∞
Pressure gradient along the streamwise direction	$\frac{\partial P}{\partial x}$	$\frac{q_\infty}{D}$

170 flow profiles (mesh points in a line in the wall-normal direction) are collected along the emerging cylinder from the S3Ch ZDES computation to build the training dataset (see section III A). For each simulation of the NASA model 11 configuration (namely ZDES, RANS SA and RANS SAR), the corresponding testing set is made of 39 flow profiles located in the separating/reattaching flow region, interpolated at the same y/h positions as in the training case, with $h = D - d$ the height of the step. Each flow profile is made of 105 values. The sensitivity of the model to the number of points in the input flow profiles has not been studied, but the chosen number of points should not significantly influence the prediction provided that there are enough points to capture the physics of the flow in the feature maps. Conversely, too much points would unnecessarily complexify the model, involving more training parameters. The present study aims at being a proof of concept to demonstrate the potential of such an approach to predict wall-pressure fluctuations. The optimisation of the model's performance through the determination of the optimal

number of points in the input profiles are a further step of this work.

2. *Training output dataset*

For each of the 170 streamwise numerical sensors distributed along the S3Ch afterbody, the corresponding Cp_{rms} values and pressure spectra form the output training set for CNN1 and CNN2, respectively. The PSD was computed with a classical average periodogram from the pressure signals using 60 overlapping blocks, resulting in a frequency resolution of 152 Hz (*i.e.* $St_D = 0.087$). The frequency resolution has been chosen low enough (in average over 60 blocks) in order to obtain a relatively smooth spectrum in the training process. Each spectrum in the training database was uniformly sampled in a log-scaled frequency range, resulting in an output vector with 67 values of the normalised PSD.

C. CNNs architectures and training

In this work, two 1D convolutional neural networks are developed for the prediction of wall-pressure fluctuations in separating/reattaching flows. The developed CNNs learn a mapping between the input mean flow profiles (see Table. III) and Cp_{rms} (CNN1) and the wall-pressure spectrum (CNN2) for a given streamwise location. Before describing the architecture of the present CNNs, let us briefly recall the principle of CNNs.

1. *Details on convolution neural networks*

CNNs were first proposed by LeCun *et al.*[62] to overcome the limitations of classical Multi-Layer Perceptrons (MLP) to treat grid-like data. Indeed, the use of MLPs to treat high-dimensional input data involves too many trainable parameters. CNNs are more efficient as they require fewer parameters, and are known for their ability to extract spatial features from input data[45,58,104]. Therefore, this study aims to exploit these characteristics to map the relationship between the spatial evolution of mean flow variables and the fluctuating pressure at the wall.

CNNs consist of three types of layers: convolutional layers, pooling layers and fully connected layers. In 1D-CNNs, the convolutional layer, usually followed by a nonlinear activation function f, computes a so-called output feature map from an input layer as:

$$\mathbf{y_i^c} = f(\mathbf{k_i} * \mathbf{x^c} + b_i^c) \quad , \quad i = 1, \dots, K \tag{5}$$

where $\mathbf{x^c}$ is the input feature map with size $H \times D$ (heigth H and depth D), $\mathbf{k_i}$ is the i^{th} convolution kernel with dimensions $F \times D$, b_i^c is the i^{th} bias (scalar) and $\mathbf{y_i^c}$ the i^{th} output feature map, namely a vector of size $P = \frac{H-F}{S} + 1$ with S the stride. Finally,$*$ denotes the convolution operator. A total of K output vectors are computed, with K the number of kernels. The convolution process is illustrated in Fig. 16. To perform the convolution operation between the kernel $\mathbf{k_i}$ and the input $\mathbf{x^c}$, each element of the output vector y_i is computed by dot product of $\mathbf{k_i}$ and a subset of the input matrix of size $F \times D$. By sliding the kernel window along $\mathbf{x}$ with stride S, the whole output feature map $\mathbf{y_i^c}$ is obtained.

The pooling layer follows a convolutional layer and aims to reduce the dimension of data while preserving the detected features. In this study, max-pooling is employed. As illustrated in Fig. 16, it consists in extracting the maximum value in the pooling window of size L sliding along the vector $\mathbf{y_i^c}$ with stride S. It allows to avoid overfitting and to reduce the number of parameters in the network. Overfitting means that the model performs well on the training set but poorly on unknown data.

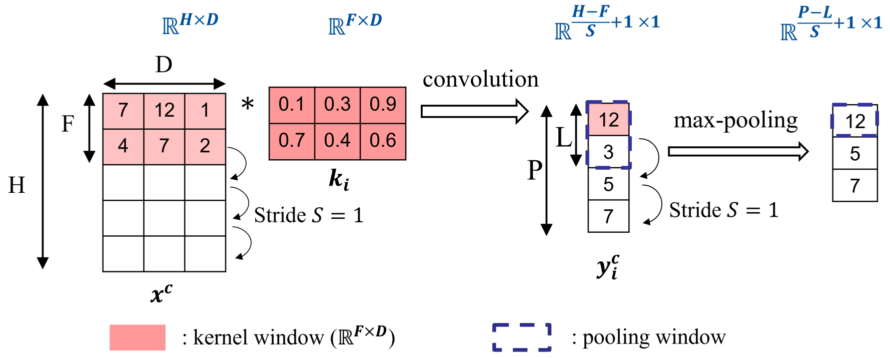

FIG. 16: Sketch of the convolution and max-pooling process used in the architecture detailed in Fig. 18 with a single kernel. In this example, $D = 3$, $H = 5$, $F = 2$, $L = 2$, $S = 1$, $P = \frac{H-F}{S} + 1$.

Finally, in most of CNNs, one or several fully connected layers precede the output (see Fig. 18 for the present case). Each artificial neuron in a fully connected layer (also called dense layer) is connected to all the neurons of the previous layer, as illustrated in Fig. 17. An artificial neuron computes a weighted sum of the components of the input vector $\mathbf{x^f}$, adding a bias b^f and applying an activation function f. Thus, the output y_i^f of the i^{th} neuron in a fully connected layer is a scalar given by:

$$y_i^f = f(\sum_{k=1}^{N} w_k x_k + b^f) \tag{6}$$

with N the number of neurons in the preceding layer and $\mathbf{w} = [w_1, ..w_N]$ the weight vector.

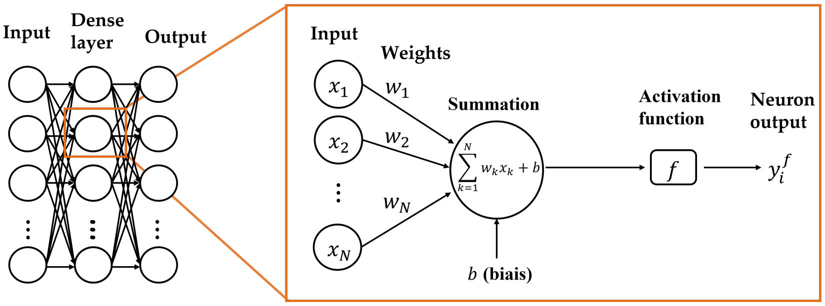

FIG. 17: Fully-connected layer along with the description of an artificial neuron.

The kernel values, the biases and the weights are the learnable parameters, optimised during the training process.

2. *Architectures of the CNNs and hyperparameters setting*

In this study, two CNNs were designed for the prediction of Cp_{rms} (CNN1) and the associated pressure spectra (CNN2), respectively. The chosen architecture for each CNN is detailed in Fig. 18. The input layer is a 2D matrix whose columns are the profiles of each input feature after applying standardisation, e_i referring to the i^{th} standardised input feature. Following this input layer, both CNNs share a common succession of three convolutional/max-pooling layers. The choice of the number of convolutional layers and kernels, as well as the sizes of the kernels and pooling windows, was inspired by a literature review of previous studies using CNNs for regression problems in aerodynamics.[49,51,53,105] These parameters are reported in Table IV. The output layers are, respectively, a scalar and a vector corresponding to the predicted Cp_{rms} and pressure spectrum before rescaling in physical units. The rectified linear unit activation function

($ReLU(x) = max(0,x)$) is used for each convolutional and fully-connected layer. $ReLU$ is a widely used activation function due to its ability to train the networks faster[51,106].

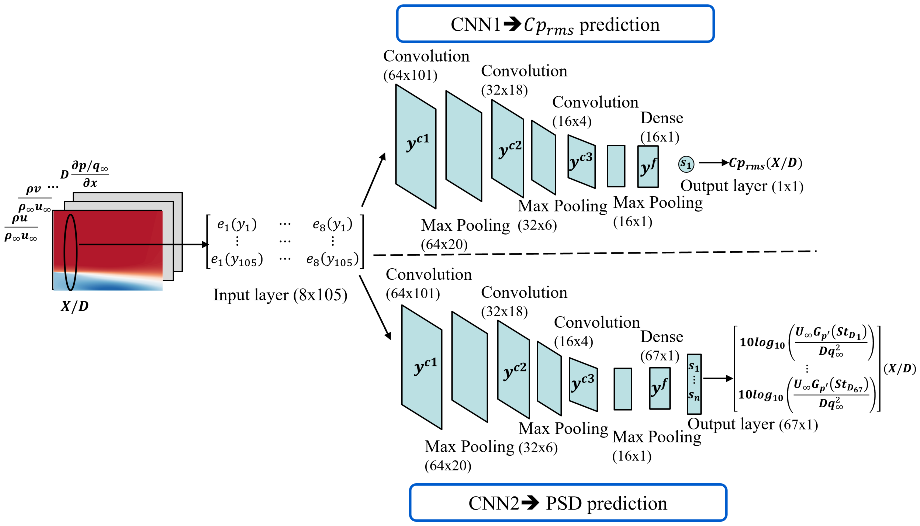

FIG. 18: Architectures of the two convolutional neural networks (CNN1 and CNN2 as introduced in Fig. 15) used for the prediction of Cp_{rms} and pressure spectra. $\mathbf{y^{ci}}$ denotes the output of the i^{th} convolutional layer, and $\mathbf{y^{f}}$ denotes the output of the fully-connected layer.

TABLE IV: Parameters of the convolutional and pooling layers

Layer	Kernel size (K)	Number of kernels (L)	Size of pooling window (P)	Output shape
1st convolution / pooling	64	5	-	64×101
1st pooling	-	-	5	64×20
2nd convolution	32	3	-	32×18
2nd pooling	-	-	3	32×6
3rd convolution	16	3	-	16×4
3rd pooling	-	-	3	16×1

The training was performed using Adam optimiser[107] (stochastic gradient descent). The mean-

Accepted to Phys. Fluids 10.1063/5.0146358

squared error was selected as loss function J:

$$J(\mathbf{s},\bar{\mathbf{s}}) = \frac{1}{n}\sum_{i=1}^{n} |s_i - \overline{s_i}|^2 + \lambda ||\mathbf{w}||_2 \tag{7}$$

with n the size of the output layer, $\mathbf{s}$ and $\bar{\mathbf{s}}$ the predicted and true n-dimensional vectors, respectively, and λ a regularisation parameter to avoid overfitting. L_2 regularisation penalises largest weights using the L_2 norm. The regularisation parameter is set to $\lambda = 0.01$.

The dataset was split into 80% for training and 20% for validation, and early stopping was used to prevent overfitting[108]. Early stopping allows to interrupt the training process when the validation loss reaches a steady state.

IV. PHYSICAL INTERPRETABILITY OF THE CNNS

This section aims to bring insights to understand how the present CNNs process the data in their hidden layers and build a mapping between the input mean flow profiles and the output quantities characterising pressure fluctuations. This exercise is rarely addressed in the fluid mechanics literature involving CNNs[109].

A. Flow features identification

A feature maps analysis of the intermediate outputs from the hidden layers allows to show that the CNNs identify characteristic patterns in the flow field. First, plots of the 8 input variables for both training and testing cases are displayed in Fig.19. One can observe that the physics of the flow is similar in both cases: the input flow field presents similar characteristics identified in these plots such as a shear layer, a recirculation zone and a reattachment region characterised by high pressure levels. Let us be reminded that the ability of CNNs to extract spatial features from an input is precisely the salient asset of the method we are looking for.

Figures 20, 21 and 22 show examples of concatenated outputs of the three convolutional layers of network CNN1 for both training and testing cases. These intermediate outputs are the so-called feature maps. Each one corresponds to a specific kernel and highlights the flow features detected through the convolution process. Figures 20a, 21a and 22a display feature maps obtained for the S3Ch test case and figures 20b, 21b and 22b show the corresponding feature maps for the NASA model 11 test case. One can note that for a given kernel, similar features such as the shear layer, recirculation or reattachment zones are detected and their location identified in both cases (see red squares in the figures). In addition, it is observed that the same features are detected in the three convolutional layers, suggesting that the same information is propagated from one layer to another. The features that are evidenced clearly correspond to those visible on the input datasets in Fig. 19. It shows that the trained CNN is able to identify and locate the typical topological features of separating/reattaching flows.

Quantitative comparisons between feature maps of training and testing cases can also be provided. Following Lee and You[109], we define the size of information I for a given feature map as:

$$I = \sqrt{\sum_{i,j}^{n_x,n_y} F_{ij}^2} \tag{8}$$

with i, j the pixel indices, n_x, n_y the number of pixels in each direction and $F_{ij} \in [0;1]$ the value of the corresponding pixel (ranging between 0 (black cell) and 1 (white cell)). In the following we use the relative size of information I_{rel} in a feature map on a given layer:

$$I_{rel} = I/I_{max} \tag{9}$$

with I_{max} the maximum size of information among all feature maps in the layer.

The relative size of information in each feature map calculated for both cases (*i.e.* S3Ch and Model 11) and for the three convolutional layers are plotted in Fig. 23a, 23b and 23c. Each point corresponds to a specific feature map identified by its index. For all layers, the relative size of information in all feature maps for training and application cases are very close. This suggests that similar features are detected through the convolution process in both cases and supports the qualitative analysis of figures 20, 21 and 22.

B. Relative contribution of input variables

This section aims to analyse the contribution of each input variable to the feature maps introduced in section IV A. Following the work by Lee and You[109], the contribution of an input variable is identified by feeding the CNN with only one variable, the other components of the input matrix being set to zero.

Let I_i be the size of information (see Eq. 8) in a given feature map calculated with the variable i only. The contribution factor CF of this variable i is defined as:

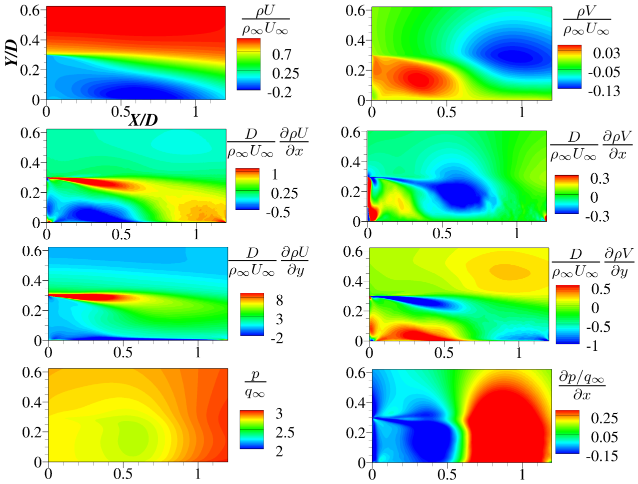

(a) Training case (S3Ch)

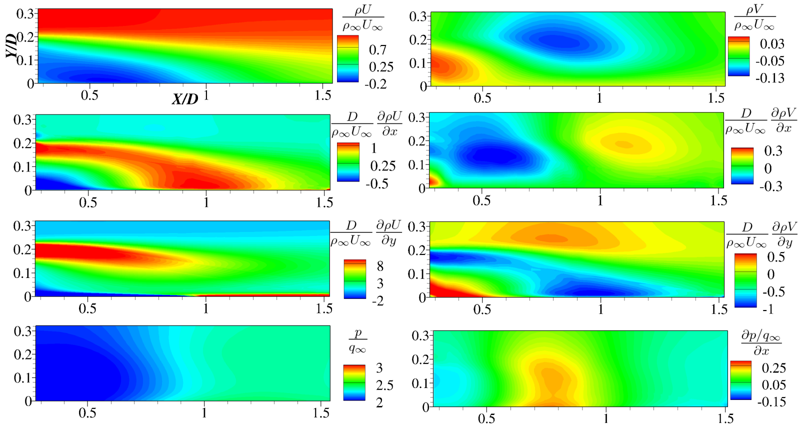

(b) Testing case (NASA Model 11)

FIG. 19: Mean fields of input variables.

$$CF_i = \frac{I_i}{\sum_{k=1}^{n_{var}} I_k} \tag{10}$$

with n_{var} the number of input variables ($n_{var} = 8$ in the present case).

The contribution factor of a variable represents the relative contribution of this variable to the

Accepted to Phys. Fluids 10.1063/5.0146358

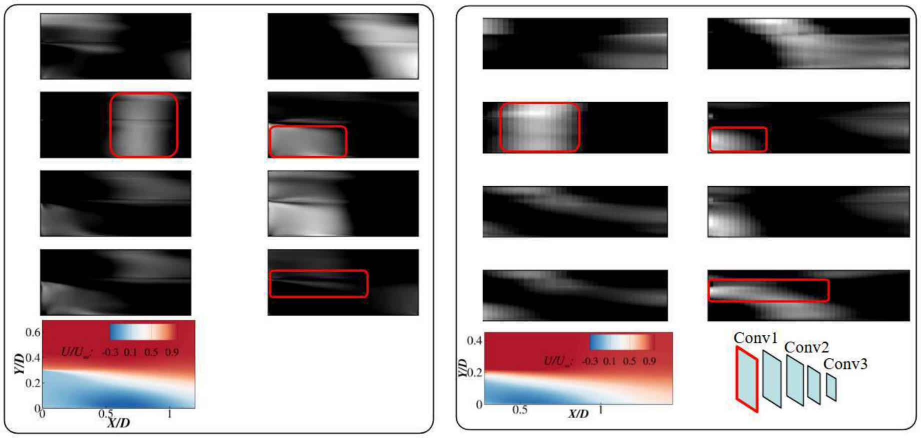

(a) Training case (S3Ch)

(b) Testing case (NASA Model 11)

FIG. 20: Feature maps obtained after the first convolutional layer. (a) Training case (S3Ch). (b) Testing case (NASA Model 11). Similar patterns in both cases corresponding respectively to the recirculation, the shear layer and the reattachment regions are detected by the convolution process (red rectangles).

total amount of information contained in a feature map. In a given layer, this factor has been calculated for each feature map and all variables. The frequency distribution and associated probability density functions (PDF) of the contribution factor for the eight variables in the first convolutional layer and both test cases are plotted in Fig. 24. The PDFs show a maximum around 0.125 in average, corresponding to one divided by the number of variables. It means that all input variables contribute equally to the prediction. Though not shown here, a similar behaviour is observed for layers 2 and 3. Besides, the PDFs and the frequency distributions obtained for the training and testing cases are very close. This provides an additional quantitative evidence that the CNN identifies similar features in both flow fields.

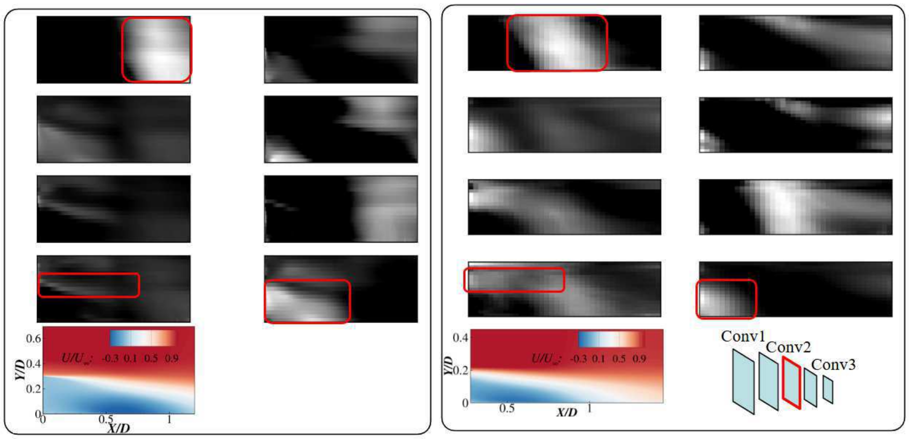

(a) Training case (S3Ch)

(b) Testing case (NASA Model 11)

FIG. 21: Feature maps obtained after the second convolutional layer.

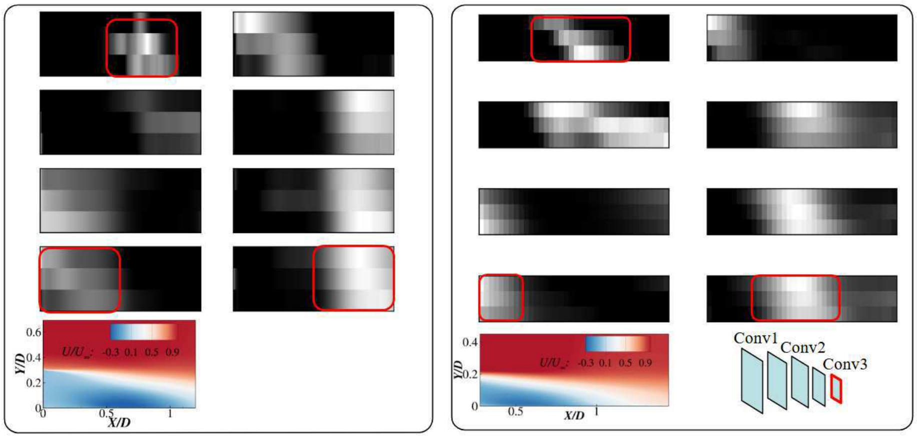

(a) Training case (S3Ch)

(b) Testing case (NASA Model 11)

FIG. 22: Feature maps obtained after the third convolutional layer.

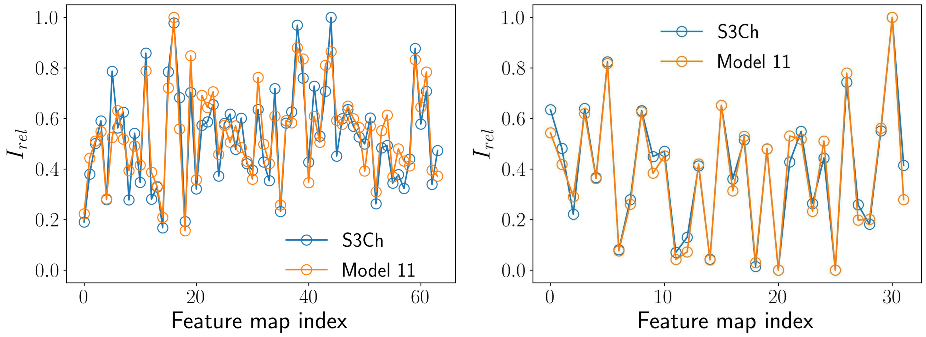

(a) Layer 1

(b) Layer 2

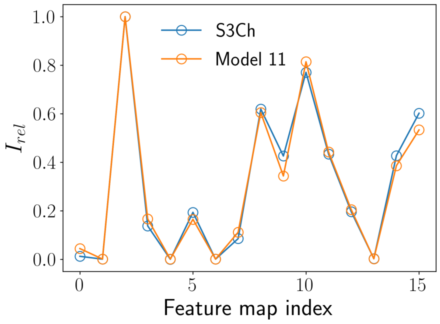

(c) Layer 3

FIG. 23: Relative sizes of information in feature maps of the three convolutional layers of CNN1 calculated for the S3Ch and Model 11 test cases.

V. RESULTS

A. Training of the CNNs

First, the evolution of the training and validation loss functions with respect to the training epochs is displayed in Fig. 25 for both trained CNNs. Thanks to the early stopping criterion, it can be seen that training ends when the validation loss stops decreasing, preventing overfitting to occur. The training time for CNN1 and CNN2 was 242 s and 248 s, respectively.

The true and learned fluctuating pressure coefficients and dimensionless PSD are compared in Figs 26 and 27 at 9 streamwise locations ($X/D = [0.1, 0.3, 0.5, 0.6, 0.7, 0.8, 0.9, 1, 1.1]$). The

Accepted to Phys. Fluids 10.1063/5.0146358

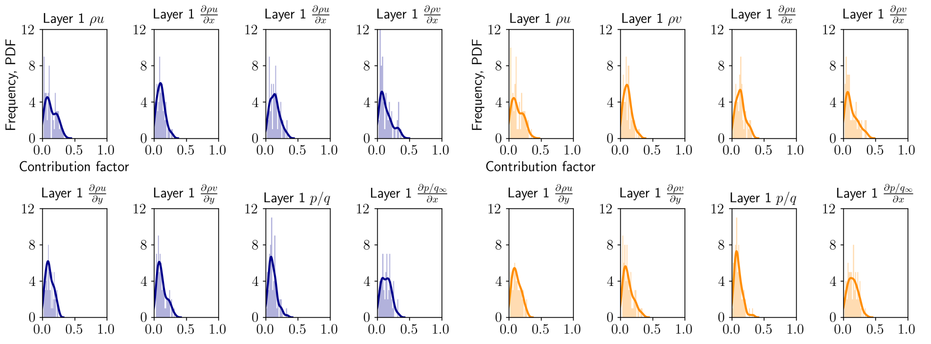

(a) (b)

FIG. 24: Histograms of frequencies and PDFs (solid lines) of input flow variables as a function of the contribution factors of the input variables calculated on the feature maps of the first layer of CNN1 for the S3Ch training case (a) and the Model 11 testing case (b).

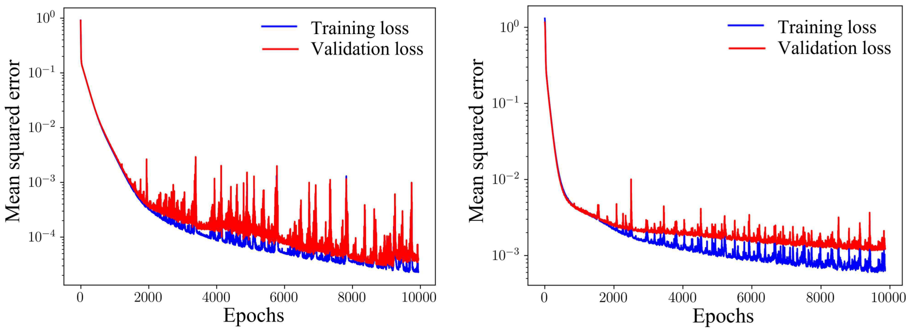

(a) (b)

FIG. 25: Evolution of the training and validation loss functions during training of CNN 1 (Fig.25a) and CNN 2 (Fig. 25b).

learned and reference curves are almost superimposed, which means that the present models successfully learned the evolution of Cp_{rms} and the power spectral density of pressure fluctuations at the wall.

Accepted to Phys. Fluids 10.1063/5.0146358

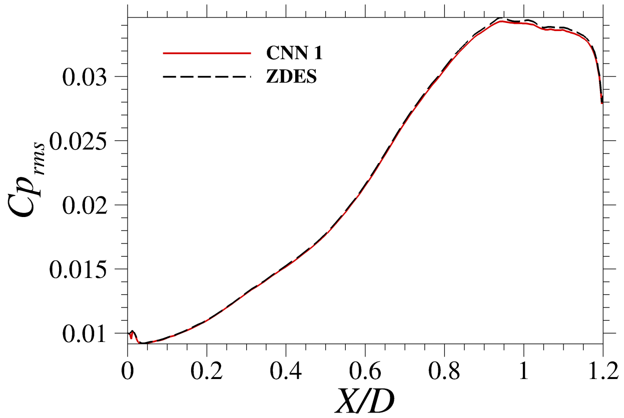

FIG. 26: True and learned evolutions of the fluctuating pressure coefficient for the training case (CNN1).

B. Prediction on the NASA model 11 test case

The trained models described in sub-section A have then been applied on the testing dataset corresponding to the ZDES time-averaged flow field in the separating/reattaching flow region of the NASA Model 11 launcher (referred to as M11 in the following). We first focus on the prediction of Cp_{rms} using CNN1.

1. Cp_{rms} prediction

As explained in section III A, the predicted Cp_{rms} is obtained after rescaling the CNN's output in physical units by applying the inverse standardisation operation (*i.e* multiplying by the standard deviation σ and adding the mean μ of training output data). Due to the limited available database used to train the network, that contains mean flow profiles and corresponding Cp_{rms} values taken from a unique configuration with specific flow conditions, the training process is inevitably biased, and the predicted Cp_{rms} magnitude is imposed by the training configuration. The predicted evolution of Cp_{rms} for the testing case is plotted in Fig. 28 (dotted line). It is observed that our model is able to predict the relative evolution of this quantity along the streamwise direction and to accurately locate the position of the peak corresponding to the maximum of pressure fluctuations.

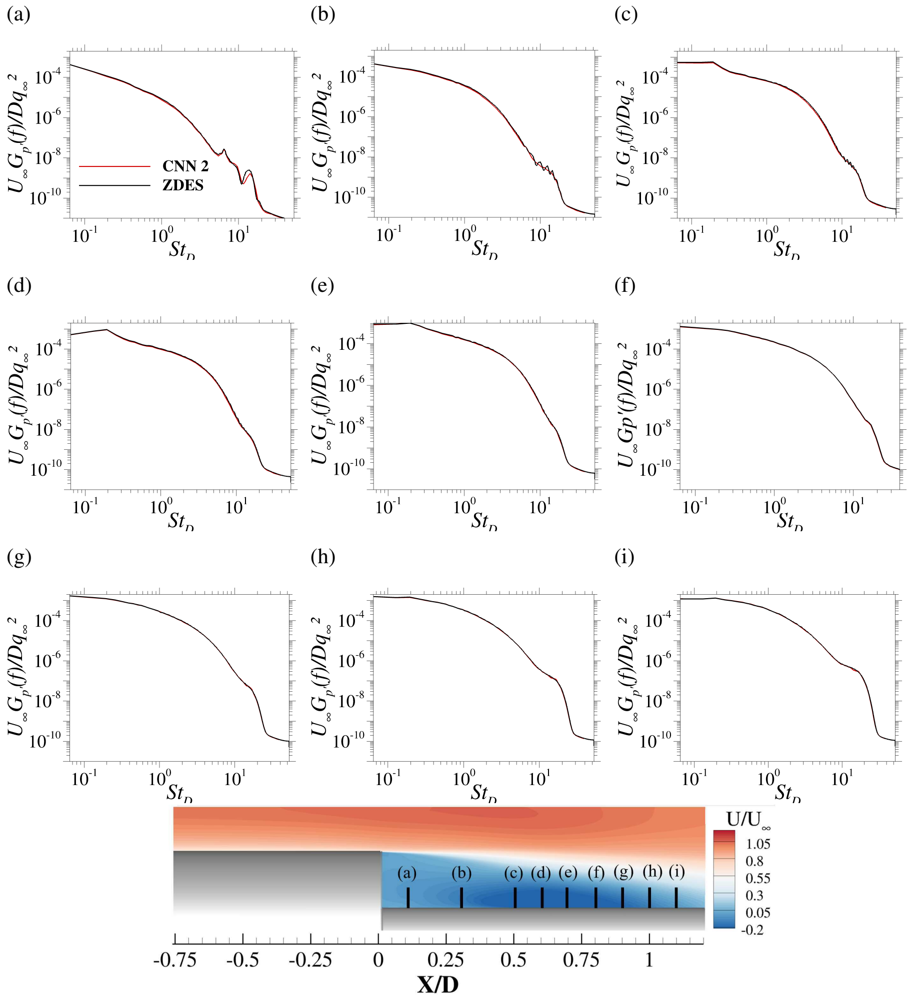

FIG. 27: True (—) and learned (—) spectra for the training case at 9 streamwise positions (CNN2).

However, the predicted levels are wrong as the output's mean value and standard deviation are driven by the training data. Indeed, our trained model cannot be expected to generalise and infer the pressure fluctuations levels to very different flow conditions and geometries, but only to detect similarities in the flow and thus predict the relative evolution of output quantities. It is expected that this bias would be eliminated by enriching the training dataset with multiple configurations. Building such a database would require a significant time and computational cost. However, as shown in the following, the present work allows to demonstrate the interest of the strategy.

The capability of our model to identify the zones of high pressure fluctuations and predict the relative evolution of the RMS pressure coefficient is illustrated in the Fig. 28 (continuous red line). The CNN's output is scaled using the mean and standard deviation values computed from the testing case (these values being supposed to be unknown in the general case). The correct magnitudes are then retrieved, with an average error between the prediction (red line) and the reference ZDES data (black line) $\Delta Cp_{rms}|_{CNN/ZDES} = ||(Cp_{rms})|_{CNN} - (Cp_{rms})|_{ZDES}||/(Cp_{rms})|_{ZDES} = 18\%$. The average error with respect to the measurements is $\Delta Cp_{rms}|_{CNN/Exp} = 9\%$. It is of major importance to note that this rescaling procedure only affects the overall levels of the Cp_{rms} curve. The position of the RMS-pressure peak and the general evolution of this quantity are accurately predicted by the initial neural network CNN1.

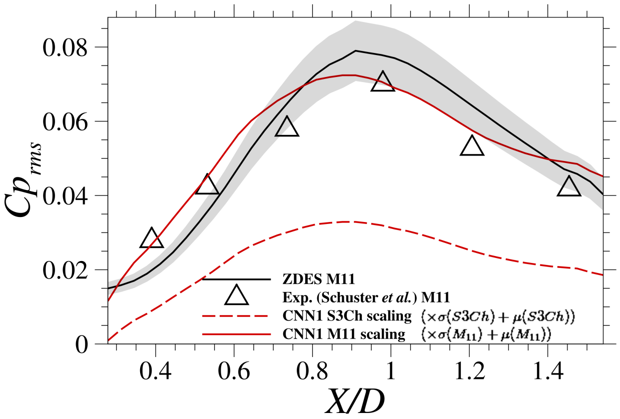

FIG. 28: Predicted evolution of the fluctuating pressure coefficient along the wall using inverse standardisation based on the training configuration S3Ch (—) and on the testing configuration M11 (– –). μ and σ refer respectively to the mean and standard deviation of Cp_{rms} computed using the ZDES data in the domain of study. The grey area represents 10% difference with respect to the reference ZDES data.

To overcome the issue of underprediction of the fluctuation levels, this study proposes a general scaling procedure to retrieve accurate output magnitudes. The output of CNN1 is the RMS pressure coefficient, namely the ratio of the RMS pressure with respect to the free stream dynamic pressure: $Cp_{rms} = \frac{P_{rms}}{q_\infty}$. Because of the standardisation procedure, the predicted and the training fluctuating pressure coefficient magnitudes are approximately equal:

$$Cp_{rms}|_{M11}^{predict} = \left.\frac{P_{rms}}{q_\infty}\right|_{M11}^{predict} \sim \left.\frac{P_{rms}}{q_\infty}\right|_{S3Ch} \qquad (11)$$

To account for the testing case flow conditions and rescale the CNN's output consequently, we propose the following scaling procedure, adapted from the work of Panda *et al.*[110]:

$$Cp_{rms}|_{M11}^{rescaled} = Cp_{rms}|_{M11}^{predict} \times \frac{q_\infty|_{M11}}{q_\infty|_{S3Ch}} \qquad (12)$$

These authors compared two wind tunnel tests of the NASA Model 11 configuration using a scaling factor. Such a treatment permits to account for the difference in the dynamic pressure between the two experiments, assuming that the magnitude of pressure fluctuations is proportional to the free-stream dynamic pressure and that the power spectral density is proportional to q_∞^2.

Figure 29 shows the Cp_{rms} curves obtained after applying the proposed scaling factor on the CNN's output (red dotted line in figures 28 and 29). The resulting Cp_{rms} levels (blue curve in Fig. 29) are slightly overestimated with respect to the reference ZDES and experimental data, with average deviations of 25% and 29% compared to the ZDES results and the experimental data, respectively, but represent a significant improvement compared to the original raw output.

As the trained CNNs only need mean flow profiles to predict fluctuating quantities, it would be beneficial in terms of computational cost to build the input dataset for a given application case using RANS simulations instead of ZDES. As a consequence, the influence of the turbulence model used to produce the input mean flow field is investigated in the following. In Fig. 30, predicted Cp_{rms} curves using ZDES, RANS Spalart-Allmaras model (SA) and RANS Spalart-Allmaras with rotation correction (SA-R) to provide the input flow field are plotted and compared to available experimental data by Schuster *et al.*[74] and the reference ZDES results. These predictions are obtained using the same CNN trained with the ZDES time-averaged flow field of the S3Ch configuration. The scaling based on expression (12) is used.

In Fig. 30, one can see that the three curves obtained using ZDES, RANS SA and RANS SA-R data are quite close. The average errors are $\Delta Cp_{rms}|_{CNN1/ZDES} = 31\%$ and $\Delta Cp_{rms}|_{CNN1/Exp} = 27\%$ using the SA input data versus $\Delta Cp_{rms}|_{CNN1/ZDES} = 30\%$ and $\Delta Cp_{rms}|_{CNN1/Exp} = 31\%$ with the SAR input data, respectively. This demonstrates that the prediction is not very sensitive to the turbulence model used to generate the input flow field of an untried configuration. This is of major

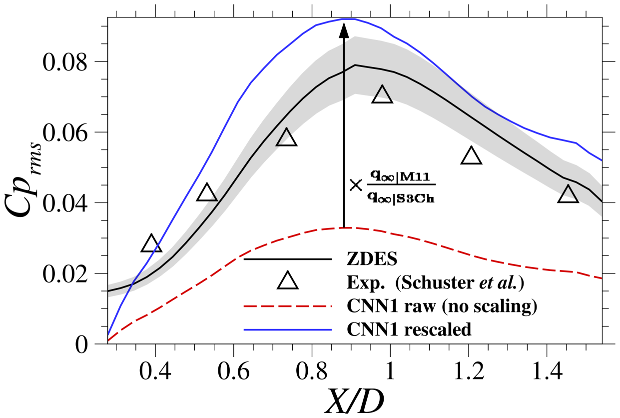

FIG. 29: Predicted evolution of the fluctuating pressure coefficient along the wall using training case for inverse standardisation(– –) and the proposed scaling procedure (—). The grey area represents 10% difference with respect to the reference ZDES data.

importance regarding the computation cost of the whole prediction process: for a given test case, one only needs a single RANS simulation to get a fair estimate of the evolution of the fluctuating wall-pressure. This represents an outstanding gain in terms of computational resources in the global prediction process, provided that the studied configuration features a separating/reattaching flow and that an adapted scaling procedure is used.

2. *Pressure spectra prediction*

For the same reason mentioned in section V B 1 (scaling of data using the training configuration), the predicted dimensionless power spectral density of pressure fluctuations obtained by applying CNN2 on the ZDES time-averaged flow field of the testing configuration are underpredicted (see Fig. 31). Following the same approach as in section V B 1, a scaling procedure has been proposed for the PSD predicted by the corresponding trained CNN. The analogous scaling is:

$$\left.\frac{U_\infty G_{p'}(f)}{Dq_\infty^2}\right|_{M11}^{rescaled} = \left.\frac{U_\infty G_{p'}(f)}{Dq_\infty^2}\right|_{M11}^{predict} \times \frac{\left.\frac{q_\infty^2 D}{U_\infty}\right|_{M11}}{\left.\frac{q_\infty^2 D}{U_\infty}\right|_{S3Ch}} \qquad (13)$$

As the power spectral density unit is Pa^2/Hz, the proposed scaling for the dimensionless PSD

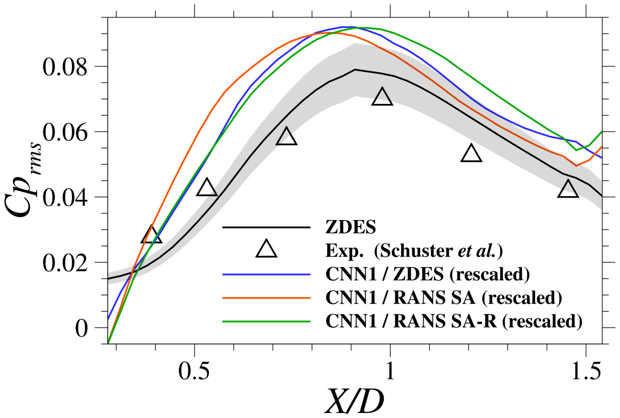

FIG. 30: Predicted evolution of the fluctuating pressure coefficient along the wall using ZDES (—), RANS SA (—) and RANS SAR (—) flow fields as input and applying the proposed scaling factor. Predicted Cp_{rms} are compared to the reference ZDES results (—). The grey area represents 10% difference with respect to the reference ZDES data.

is based on the squared ratio of free stream pressures[110] and the ratio of reference diameters with respect to free stream velocities for each case, namely S3Ch and M11.

Dimensionless PSD predicted at streamwise position $X/D = 1.1$ by the CNN is plotted in Fig.31 with (blue line) and without (red line) scaling. This corresponds to the reattachment region, experiencing the highest pressure fluctuations. These curves are compared to the spectrum obtained by ZDES (black line). Similarly to what was observed with CNN1 for the evolution of Cp_{rms}, the shape of the predicted spectrum seems well predicted, but the PSD magnitude is greatly underestimated. After scaling (Eq. 13), the predicted spectrum fits the reference spectrum in a broad range of Strouhal numbers ($St_D \simeq 0.5-20$), emphasised by the black dotted lines in Fig. 31. In the low frequency range, the CNN overpredicts the PSD. This gap may originate from a lack of training data in this frequency range. Indeed, due to the limited time of simulation (200 ms or $tU_\infty/D = 348$), few points are available to train the model at low frequencies. The prediction of the power spectral density at very low frequencies would require the computationally expensive acquisition of longer pressure signals. In this context, robust and highly validated hybrid RANS/LES methods such as ZDES mode 2 (2020) are interesting tools to compute low frequency spectra with limited time and resources. In the high frequency range, a sudden drop of the predicted PSD is observed after $St_D = 20$, and no data is plotted after $St_D = 50$. Indeed, as stated in section II A, training data were acquired at a sampling frequency of 250 kHz ($St_D = 105$). The CNN was therefore trained with frequencies less than 125 kHz according to the Nyquist-Shannon criterion, corresponding to Strouhal numbers less than 52. Hence, no PSD value can be predicted for higher Strouhal numbers with the present CNN. In practice, it is not an issue: from the reference ZDES computation, one gets $\int_0^{52} G_{p'}(St_D)dSt_D / \int_0^{\infty} G_{p'}(St_D)dSt_D = 0.999$.

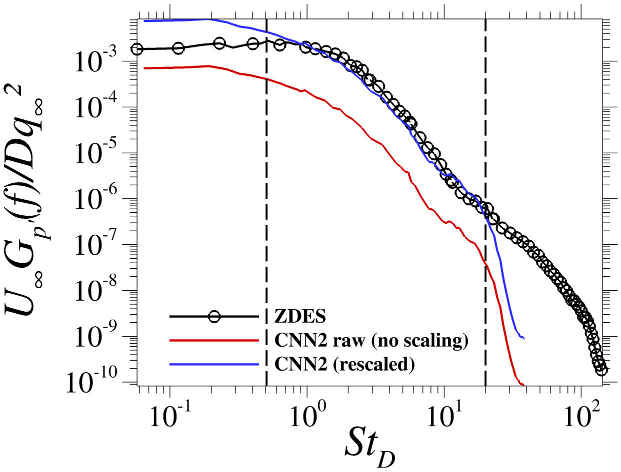

FIG. 31: Predicted wall pressure spectra at $X/D = 1.1$ with (—) and without (—) scaling compared to the ZDES reference (-○-). The black dotted lines highlight the limits of the frequency range where the model performs well ($St_D \in [0.5 - 20]$).

Figure 32 shows the scaled pressure spectra predicted by CNN2 based on ZDES, RANS SA and RANS-SAR data, compared to the pressure spectra computed with ZDES at several streamwise positions. The same trend is observed: the predicted spectra are marginally influenced by the input turbulence model and they fit quite well the reference spectra in the medium Strouhal range ($0.7 < St_D < 20$). The dimensionless PSD $\frac{U_\infty G_{p'}(f)}{Dq_\infty^2}$ is overestimated in the low frequency range ($St_D < 0.7$) and underestimated in the high frequency band ($St_D > 20$). However, the contribution of PSD values beyond $St_D = 50$ to the RMS pressure is negligible. Finally one can note that the quality of the predictions is decreased at the beginning (Fig 32a) and at the end (Fig 32i) of the domain. Indeed, the flow field for both streamwise positions is quite different from the

S3Ch training case. In the training case, the flow separation is caused by a sudden expansion. In the application case, an inclined wall follows the separation point. One can assume that this geometric difference has a significant influence on the mean flow field at the beginning of the working domain, impacting the CNN's prediction. Finally, the spectrum of Fig 32i has been calculated for a streamwise position located after the reattachment region. However, the training domain in the S3Ch case stops immediately after reattachment. The CNN was therefore not trained for this area of the flow.

Finally, Fig. 33 displays the predicted dimensionless power spectral density map scaled with equation 13 (a) compared to the reference PSD map resulting from the ZDES simulation (b). As it was shown in figures 31 and 32, levels of dimensionless PSD are overestimated for low Strouhal numbers by CNN2. This leads to a characteristic pattern of larger width compared to L for the reference ZDES computation, and related to high-energy low frequencies. This spatial extent of high pressure fluctuations is caused by the oscillation of the reattachement point around its mean position[12]. However, this region is accurately located and centered around $X/D \simeq 0.85$ by the current CNN. At the end of the domain, the CNN still predicts overestimated high pressure fluctuations levels at low frequencies. As stated previously, such an observation could be explained by the fact that the CNN was not trained for this region of the flow.

Regarding the frequency distribution of the energy of pressure fluctuations, similar characteristic frequency bands are predicted by the CNN (domains 1, 2 and 3 in Fig.33). At low frequencies, high level pressure fluctuations originate from the impact of turbulent structures on the wall and from the flapping motion of the shear layer[12,72]. At higher frequencies, one can suggest that the PSD map reveals the wall signature of the high frequency fluctuations originating from the growing vortices in the shear layer[71,72]. This study shows that the spatial evolution of the fluctuating pressure field can be predicted from a simple mean flow field.

VI. CONCLUSION

In this work, we developed two Convolutional Neural Networks to predict the evolution of the fluctuating wall-pressure coefficient and associated pressure spectra for separating/reattaching transonic flows. The models were trained using a ZDES simulation of a generic axisymmetric afterbody configuration and applied on a semi-realistic launcher geometry. ZDES is a powerful tool to provide training samples of physical data such as low-frequency power spectral density at

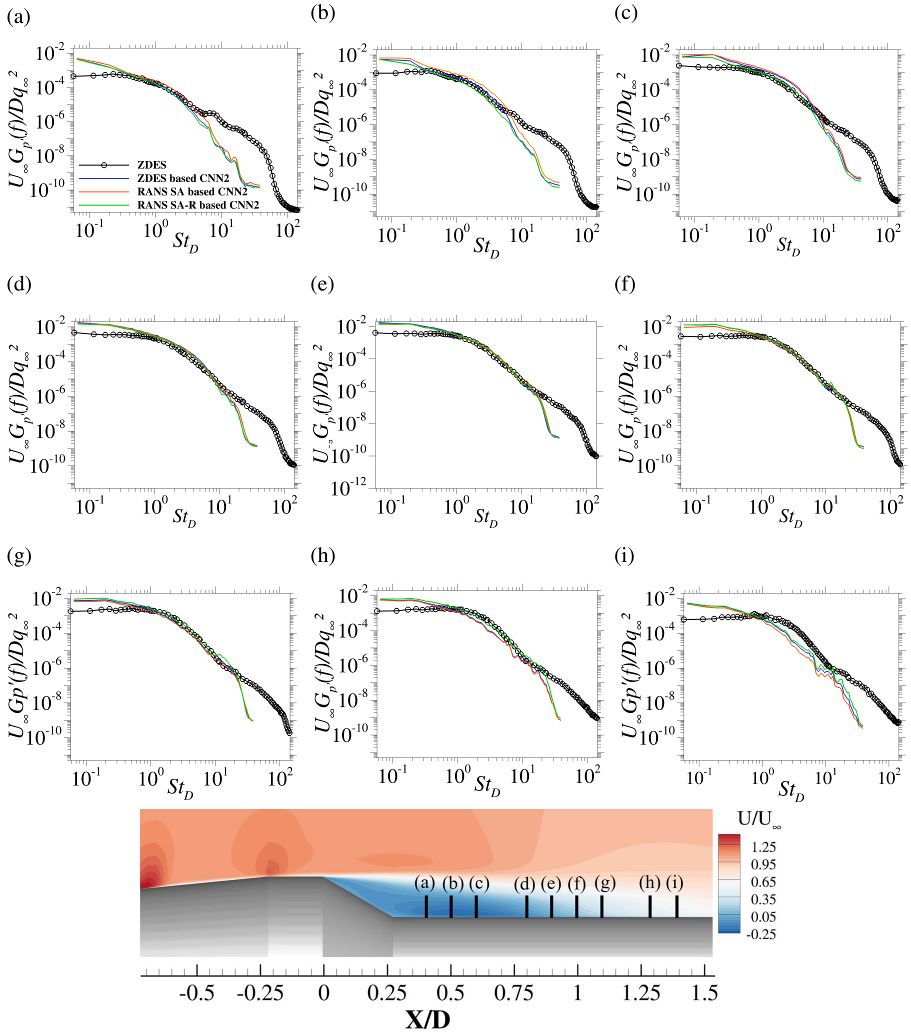

FIG. 32: Rescaled predicted wall-pressure spectra at different streamwise positions with CNN2 using ZDES (—), RANS SA (—) and RANS SA-R (—) flow fields as input compared to reference ZDES results (—).

a limited computational cost.

Comparison with ZDES results showed that our trained models are able to infer the relative

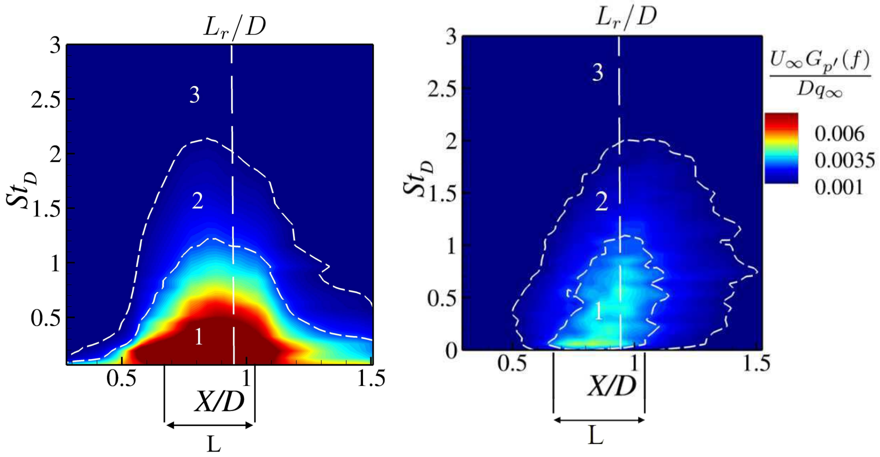

(a) (b)

FIG. 33: Rescaled predicted (a) and ZDES (b) power spectral density (PSD) maps of the fluctuating pressure. The reattachment location normalised by the reference diameter L_r/D is highlighted by a white dotted line.

evolution of the predicted quantities and to accurately locate the zone of highest pressure fluctuations, using only mean flow data as inputs. In section IV, we gave some insights to understand how the CNNs process the data in their hidden layers by providing feature maps resulting from the convolution operations and analyzing the information contained in it. We demonstrated that the CNN identifies patterns corresponding to physical regions of the flow (recirculation zone, reattachment region, shear layer) and relates the location and size of these patterns to output quantities thanks to the fully connected layer.

In addition, the application of the trained models on input data obtained using RANS SA and RANS SA-R simulations showed that the results marginally depend on the turbulence model used to get the input mean flow field. This result is of particular interest as it suggests that costly unsteady simulations such as ZDES are not always mandatory to provide the input mean flow fields, as similar results are obtained using RANS simulations that are less expensive. This paves the way for an efficient and time-saving method for predicting the fluctuating wall quantities of turbulent flows, especially during the design phase.

A current limitation of our model lies in the potential lack of universality of the definition of the scaling applied to the output to retrieve accurate levels of pressure fluctuations. To achieve a proper training, input and output data are standardised. However, this prevents the CNN to generalise to configurations with very different magnitudes of input mean variables and output fluctuating quantities, although we showed that it does not impact the identification of flow features and the prediction of the relative evolution of output quantities. To account for the differences in pressure fluctuation magnitudes, scaling factors for Cp_{rms} and the PSD have been proposed based on relevant physical quantities and a literature review. They allow to retrieve magnitudes close to the reference ZDES data.

These results and their limitations open different perspectives for future works. First, the relevance of the proposed scaling factors must be assessed using other configurations. Then, the generality of our models could be improved by training the CNNs on multiple configurations with different Mach and Reynolds numbers. Finally, this work could be extended to other flow types causing high pressure fluctuations such as shock-wave oscillations or flow downstream reattachment exhibiting large-scale vortex shedding.

ACKNOWLEDGMENTS

The authors wish to thank the Centre National d'Études Spatiales (CNES) for financial support. The Ph.D. work of S. Lecler is funded by CNES and ONERA. In addition, all the people involved in the evolution of the FLU3M code are warmly thanked.

REFERENCES

[1] H. A. J. Cole, A. L. Erickson, and A. G. Rainey, "Buffeting during atmospheric ascent," Tech. Rep. NASA SP-8001 (NASA, 1964).

[2] J. A. Cockburn and J. E. Robertson, "Vibration response of spacecraft shrouds to in-flight fluctuating pressures," Journal of Sound and Vibration **33**, 399–425 (1974).

[3] I. Bolgar, *On the performance increase of future space launchers : Investigations of buffeting , its reduction via passive flow control , and the Dual-Bell nozzle concept at trans- and supersonic flight conditions*, Ph.D. thesis, Université de Munich (2019).

[4] R. Camussi, A. Di Marco, C. Stoica, M. Bernardini, F. Stella, F. De Gregorio, F. Paglia, L. Romano, and D. Barbagallo, "Wind tunnel measurements of the surface pressure fluctuations on the new VEGA-C space launcher," Aerospace Science and Technology **99** (2020), 10.1016/j.ast.2020.105772.

[5] J. Slotnick, A. Khodadoust, J. Alonso, and D. Darmofal, "CFD Vision 2030 Study: A Path to Revolutionary Computational Aerosciences," Tech. Rep. NASA/CR-2014-218178 (NASA Langley Research Center, 2014).

[6] P. R. Spalart, "Comments on the feasibility of les for wings, and on a hybrid rans/les approach," in *Proceedings of first AFOSR international conference on DNS/LES* (Greyden Press, 1997).

[7] P. R. Spalart, S. Deck, M. L. Shur, K. D. Squires, M. K. Strelets, and A. Travin, "A new version of detached-eddy simulation, resistant to ambiguous grid densities," Theoretical and computational fluid dynamics **20**, 181–195 (2006).

[8] S. Deck, "Zonal-detached-eddy simulation of the flow around a high-lift configuration," AIAA journal **43**, 2372–2384 (2005).

[9] P. É. Weiss and S. Deck, "On the coupling of a zonal body-fitted/immersed boundary method with ZDES: Application to the interactions on a realistic space launcher afterbody flow," Computers and Fluids **176**, 338–352 (2018).

[10] P.-E. Weiss, "ZDES of an Ariane 6 PPH configuration with incidence angle using zonal immersed boundary conditions," in *EUCASS 2019* (2019).

[11] G. Wang, Q. Li, and Y. Liu, "IDDES method based on differential Reynolds-stress model and its application in bluff body turbulent flows," Aerospace Science and Technology **119**, 107207 (2021).

[12] Y. Liu, G. Wang, H. Zhu, and Z. Ye, "Numerical analysis of transonic buffet flow around a

hammerhead payload fairing," Aerospace Science and Technology **84**, 604–619 (2019).

[13] S. Morilhat, *Modélisation des fluctuations de la pression pariétale d'une couche limite turbulente pour des applications en vibro-acoustique*, Ph.D. thesis, Université de Toulouse (2018).

[14] G. M. Corcos, "Resolution of Pressure in Turbulence," The Journal of the Acoustical Society of America **35**, 192–199 (1963).

[15] G. M. Corcos, "The structure of the turbulent pressure field in boundary-layer flows," Journal of Fluid Mechanics **12**, 1037 (1965).

[16] W. R. Graham, "A comparison of models for the wavenumber-frequency spectrum of turbulent boundary layer pressures," Journal of Sound and Vibration **206**, 541–565 (1997).

[17] B. Efimtsov, N. Kozlov, S. Kravchenko, and A. O. Andersson, "Wall pressure-fluctuation spectra at small backward-facing steps," in *21st AIAA Aeroacoustics Conference* (2000).

[18] J. E. Ffowcs-Williams, "Boundary-layer pressure and the Corcos model: a development to incorporate low-wavenumber contraints," Journal of Fluid Mechanics **125**, 9–25 (1982).

[19] D. M. Chase, "Modeling the wavevector-frequency spectrum of turbulent boundary layer wall pressure," Journal of Sound and Vibration **70**, 29–67 (1980).

[20] D. M. Chase, "The character of the turbulent wall pressure spectrum at subconvective wavenumbers and a suggested comprehensive model," Journal of Sound and Vibration **112**, 125–147 (1987).

[21] A. Caiazzo, R. D'Amico, and W. Desmet, "A Generalized Corcos model for modelling turbulent boundary layer wall pressure fluctuations," Journal of Sound and Vibration **372**, 192–210 (2016).

[22] S. Lee, "Empirical wall-pressure spectral modeling for zero and adverse pressure gradient flows," AIAA Journal **56**, 1818–1829 (2018).

[23] T. S. Miller, J. M. Gallman, and M. J. Moeller, "Review of turbulent boundary-layer models for acoustic analysis," Journal of Aircraft **49**, 1739–1754 (2012).

[24] M. Goody, "Empirical spectral model of surface pressure fluctuations," AIAA Journal **42**, 1788–1794 (2004).

[25] R. M. Catlett, J. M. Anderson, J. B. Forest, and D. O. Stewart, "Empirical modeling of pressure spectra in adverse pressure gradient turbulent boundary layers," AIAA Journal **54**, 569–587 (2016).

[26] Y. Rozenberg, G. Robert, and S. Moreau, "Wall-pressure spectral model including the adverse pressure gradient effects," (2014).

[27] N. Hu, “Empirical spectral model of wall pressure fluctuations including adverse pressure gradient effects,” 23rd AIAA/CEAS Aeroacoustics Conference, 2017 , 1–18 (2017).

[28] J. Robertson, “Prediction of in-flight fluctuating pressure environments including protuberance induced flow,” Tech. Rep. WR-71-10, NASA-CR-119941 (Wyle Laboratories Research Staff, Huntsville, 1971).

[29] L. J. Peltier and S. A. Hambric, “Estimating turbulent-boundary-layer wall-pressure spectra from CFD RANS solutions,” Journal of Fluids and Structures **23**, 920–937 (2007).

[30] M. Slama, C. Leblond, and P. Sagaut, “A Kriging-based elliptic extended anisotropic model for the turbulent boundary layer wall pressure spectrum,” Journal of Fluid Mechanics **840**, 25–55 (2018).

[31] G. Grasso, P. Jaiswal, H. Wu, S. Moreau, and M. Roger, “Analytical models of the wall-pressure spectrum under a turbulent boundary layer with adverse pressure gradient,” Journal of Fluid Mechanics **877**, 1007–1062 (2019).

[32] R. H. Kraichnan, “Pressure Fluctuations in Turbulent Flow over a Flat Plate,” Journal of the Acoustical Society of America, Vol. 28, No. 3, May 1956, pp. 378–390 **28**, 378–390 (1955).

[33] R. L. Panton and J. H. Linebarger, “Wall pressure spectra calculations for equilibrium boundary layers,” Journal of Fluid Mechanics **65**, 261–287 (1974).

[34] S. Remmler, J. Christophe, J. Anthoine, and S. Moreau, “Computation of wall-pressure spectra from steady flow data for noise prediction,” AIAA Journal **48**, 1997–2007 (2010).

[35] W. K. Blake, *Mechanics of Flow-Induced Sound and Vibration, vol. 1 and 2*, edited by A. P. Inc. (1986) pp. 81–177.

[36] F. Bertagnolio, A. Fischer, and W. Jun Zhu, “Tuning of turbulent boundary layer anisotropy for improved surface pressure and trailing-edge noise modeling,” Journal of Sound and Vibration **333**, 991–1010 (2014).

[37] M. Kamruzzaman, T. Lutz, W. Würz, W. Shen, W. Zhu, O. Hansen, F. Bertagnolio, and H. Madsen, “Validations and improvements of airfoil trailing-edge noise prediction models using detailed experimental data,” Wind Energy **15**, 45–61 (2011).

[38] O. Stalnov, P. Chaitanya, and P. F. Joseph, “Towards a non-empirical trailing edge noise prediction model,” Journal of Sound and Vibration **372**, 50–68 (2016).

[39] D. M. Driver, H. L. Seegmiller, and J. G. Marvin, “Time-dependent behavior of a reattaching shear layer,” AIAA Journal **25**, 914–919 (1987).

[40] K. He, X. Zhang, S. Ren, and J. Sun, “Delving deep into rectifiers: Surpassing human-level

performance on imagenet classification," in *Proceedings of the IEEE international conference on computer vision* (2015) pp. 1026–1034.

[41] Y. Goldberg, "Neural network methods for natural language processing," Synthesis lectures on human language technologies **10**, 1–309 (2017).

[42] L. Hu, J. Zhang, Y. Xiang, and W. Wang, "Neural Networks-Based Aerodynamic Data Modeling: A Comprehensive Review," IEEE Access **8**, 90805–90823 (2020).

[43] J. N. Kutz, "Deep learning in fluid dynamics," Journal of Fluid Mechanics **814**, 1–4 (2017).

[44] J. Rabault, M. Kuchta, A. Jensen, U. Réglade, and N. Cerardi, "Artificial neural networks trained through deep reinforcement learning discover control strategies for active flow control," Journal of fluid mechanics **865**, 281–302 (2019).

[45] Y. Yin, P. Yang, Y. Zhang, H. Chen, and S. Fu, "Feature selection and processing of turbulence modeling based on an artificial neural network," Physics of Fluids **32** (2020), 10.1063/5.0022561.

[46] J. Ling and J. Templeton, "Evaluation of machine learning algorithms for prediction of regions of high Reynolds averaged Navier Stokes uncertainty," Physics of Fluids **27** (2015), 10.1063/1.4927765.

[47] J. Ling, A. Kurzawski, and J. Templeton, "Reynolds averaged turbulence modelling using deep neural networks with embedded invariance," Journal of Fluid Mechanics **807**, 155–166 (2016).

[48] Y. Zhao, H. D. Akolekar, J. Weatheritt, V. Michelassi, and R. D. Sandberg, "RANS turbulence model development using CFD-driven machine learning," Journal of Computational Physics **411**, 1–19 (2020), arXiv:1902.09075.

[49] X. Jin, P. Cheng, W. L. Chen, and H. Li, "Prediction model of velocity field around circular cylinder over various Reynolds numbers by fusion convolutional neural networks based on pressure on the cylinder," Physics of Fluids **30** (2018), 10.1063/1.5024595.

[50] X. Guo, W. Li, and F. Iorio, "Convolutional neural networks for steady flow approximation," in *Proceedings of the 22nd ACM SIGKDD international conference on knowledge discovery and data mining* (2016) pp. 481–490.

[51] V. Sekar, Q. Jiang, C. Shu, and B. C. Khoo, "Fast flow field prediction over airfoils using deep learning approach," Physics of Fluids **31** (2019), 10.1063/1.5094943.

[52] N. Thuerey, K. Weißenow, L. Prantl, and X. Hu, "Deep Learning Methods for Reynolds-Averaged Navier–Stokes Simulations of Airfoil Flows," AIAA Journal **58**, 25–36 (2020), arXiv:1810.08217.

[53] S. Bhatnagar, Y. Afshar, S. Pan, K. Duraisamy, and S. Kaushik, "Prediction of aerodynamic flow fields using convolutional neural networks," Computational Mechanics **64**, 525–545 (2019), arXiv:1905.13166.

[54] K. Fukami, K. Fukagata, and K. Taira, "Super-resolution reconstruction of turbulent flows with machine learning," Journal of Fluid Mechanics **870**, 106–120 (2019), arXiv:1811.11328.

[55] Y. Zhang, W. J. Sung, and D. Mavris, "Application of convolutional neural network to predict airfoil lift coefficient," AIAA/ASCE/AHS/ASC Structures, Structural Dynamics, and Materials Conference, 2018 , 1–9 (2018), arXiv:1712.10082.

[56] K. Li, J. Kou, and W. Zhang, "Deep neural network for unsteady aerodynamic and aeroelastic modeling across multiple Mach numbers," Nonlinear Dynamics **96**, 2157–2177 (2019).

[57] L. Guastoni, A. Güemes, A. Ianiro, S. Discetti, P. Schlatter, H. Azizpour, and R. Vinuesa, "Convolutional-network models to predict wall-bounded turbulence from wall quantities," Journal of Fluid Mechanics **928** (2021), 10.1017/jfm.2021.812, arXiv:2006.12483.

[58] C. M. Ströfer, J. Wu, H. Xiao, and E. Paterson, "Data-driven, physics-based feature extraction from fluid flow fields," arXiv (2018), 10.4208/cicp.OA-2018-0035, arXiv:1802.00775.

[59] O. Levinski, "Prediction of Buffet Loads Using Artificial Neural Networks," Tech. Rep. DSTO-RR-0218 (Defence Science & Technology Organisation, 2001).

[60] J. Ling, M. Barone, W. Davis, K. Chowdhary, and J. Fike, "Development of machine learning models for turbulent wall pressure fluctuations," AIAA SciTech Forum - 55th AIAA Aerospace Sciences Meeting , 1–11 (2017).

[61] J. Dominique, J. Van Den Berghe, C. Schram, and M. A. Mendez, "Artificial neural networks modeling of wall pressure spectra beneath turbulent boundary layers," Physics of Fluids **34** (2022), 10.1063/5.0083241, arXiv:2201.03262.

[62] Y. LeCun, B. Boser, J. S. Denker, D. Henderson, R. E. Howard, W. Hubbard, and L. D. Jackel, "Backpropagation applied to handwritten zip code recognition," Neural Computation , 545–551 (1989).

[63] Y. LeCun, L. Bottou, Y. Bengio, and P. Haffner, "Gradient-based learning applied to document recognition," Proceedings of the IEEE **86**, 2278–2323 (1998).

[64] K. Fukushima, S. Miyake, and T. Ito, "Neocognitron: A Neural Network Model for a Mechanism of Visual Pattern Recognition," IEEE Transactions on Systems, Man and Cybernetics **SMC-13**, 826–834 (1983).

[65] E. Jagodinski, X. Zhu, and S. Verma, "Uncovering dynamically critical regions in near-wall

turbulence using 3D Convolutional Neural Networks," (2020), arXiv:2004.06187.

[66] D. Deprés, P. Reijasse, and J. P. Dussauge, "Analysis of unsteadiness in afterbody transonic flows," AIAA Journal **42**, 2541–2550 (2004).

[67] P. Meliga and P. Reijasse, "Unsteady transonic flow behind an axisymmetric afterbody with two boosters," in *25th AIAA Applied Aerodynamics Conference*, June (2007).

[68] S. Deck and P. Thorigny, "Unsteadiness of an axisymmetric separating-reattaching flow: Numerical investigation," Physics of Fluids **19** (2007), 10.1063/1.2734996.

[69] P. É. Weiss, S. Deck, J. C. Robinet, and P. Sagaut, "On the dynamics of axisymmetric turbulent separating/reattaching flows," Physics of Fluids **21** (2009), 10.1063/1.3177352.

[70] P. É. Weiss and S. Deck, "Numerical Investigation of the Robustness of an Axisymmetric Separating/Reattaching Flow to an External Perturbation Using ZDES," Flow, Turbulence and Combustion **91**, 697–715 (2013).

[71] R. Pain, P. E. Weiss, S. Deck, and J. C. Robinet, "Large scale dynamics of a high Reynolds number axisymmetric separating/reattaching flow," Physics of Fluids **31** (2019), 10.1063/1.5121587.

[72] L. M. Hudy, A. M. Naguib, and W. M. Humphreys, "Wall-pressure-array measurements beneath a separating/reattaching flow region," Physics of Fluids **15**, 706–717 (2003).

[73] C. F. Coe and J. B. Nute, "Steady and fluctuating pressures at transonic speeds on hammerhead launch vehicles," Tech. Rep. NASA-TM-X-778 (NASA Ames Research Center, 1962).

[74] D. M. Schuster, J. Panda, J. C. Ross, N. H. Roozeboom, N. J. Burnside, C. L. Ngo, M. Sellers, and J. M. Powell, "Investigation of Unsteady Pressure-Sensitive Paint (uPSP) and a Dynamic Loads Balance to Predict Launch Vehicle Buffet Environments," Tech. Rep. NASA/TM-2016-219352 (NASA Langley Research Center, 2016).

[75] P. Sagaut, M. Terracol, and S. Deck, *Multiscale and multiresolution approaches in turbulence* (World Scientific, 2013).

[76] F. Simon, S. Deck, P. Guillen, P. Sagaut, and A. Merlen, "Numerical simulation of the compressible mixing layer past an axisymmetric trailing edge," Journal of Fluid Mechanics **591** (2007), 10.1017/s0022112007008129.

[77] S. Deck and N. Renard, "Towards an enhanced protection of attached boundary layers in hybrid RANS/LES methods," Journal of Computational Physics **400** (2020), 10.1016/j.jcp.2019.108970.

[78] S. M. Murman and L. Diosady, "Simulation of a hammerhead payload fairing in the transonic

regime," in *54th AIAA Aerospace Sciences Meeting* (2016) pp. 1–17.

[79] S. M. Murman, P. J. Blonigan, and L. T. Diosady, "Comparison of transonic buffet simulations with unsteady PSP measurements for a hammerhead payload fairing," AIAA SciTech Forum - 55th AIAA Aerospace Sciences Meeting , 1–18 (2017).

[80] G. Wang, F. Yang, K. Wu, Y. Ma, C. Peng, T. Liu, and L. P. Wang, "Estimation of the dissipation rate of turbulent kinetic energy: A review," Chemical Engineering Science **229** (2021), 10.1016/j.ces.2020.116133.

[81] P. Spalart and S. Allmaras, "A one-equation turbulence model for aerodynamic flows," in *30th aerospace sciences meeting and exhibit* (1992) pp. 5–21.

[82] M. L. Shur, M. K. Strelets, A. K. Travin, and P. R. Spalart, "Turbulence modeling in rotating and curved channels: Assessing the Spalart-Shur correction," AIAA Journal **38**, 784–792 (2000), https://doi.org/10.2514/2.1058.

[83] S. Deck, "Recent improvements in the Zonal Detached Eddy Simulation (ZDES) formulation," Theoretical and Computational Fluid Dynamics **26**, 523–550 (2012).

[84] S. Deck and R. Laraufie, "Numerical investigation of the flow dynamics past a three-element aerofoil," Journal of Fluid Mechanics **732**, 401–444 (2013).

[85] S. Deck and J. M. Luckring, "Zonal Detached Eddy Simulation (ZDES) of the flow around the AVT-183 diamond wing configuration," Aerospace Science and Technology **57**, 43–51 (2016).

[86] P. Guillen and M. Dormieux, "Design of a 3D multidomain Euler code," in *International Seminar of Supercomputing* (Boston,USA, 1989).

[87] M.-S. Liou, "A sequel to AUSM: AUSM+," Journal of Computational Physics **129**, 364–382 (1996).

[88] I. Mary and P. Sagaut, "Large eddy simulation of flow around an airfoil near stall," AIAA journal **40**, 1139–1145 (2002).

[89] M. Pechier, P. Guillen, and R. Cayzac, "Magnus effect over finned projectiles," Journal of Spacecraft and Rockets **38**, 542–549 (2001).

[90] S. Deck, P. Duveau, P. d'Espiney, and P. Guillen, "Development and application of Spalart–Allmaras one equation turbulence model to three-dimensional supersonic complex configurations," Aerospace Science and Technology **6**, 171–183 (2002).

[91] V. Statnikov, J.-H. Meiß, M. Meinke, and W. Schröder, "Investigation of the turbulent wake flow of generic launcher configurations via a zonal RANS/LES method," CEAS Space Journal **5**, 75–86 (2013).

[92] I. Bolgar, S. Scharnowski, and C. J. Kähler, "The effect of the Mach number on a turbulent backward-facing step flow," Flow, Turbulence and Combustion **101**, 653–680 (2018).

[93] R. Kumar, P. Viswanath, and A. Prabhu, "Mean and fluctuating pressure in boat-tail separated flows at transonic speeds," Journal of Spacecraft and Rockets **39**, 430–438 (2002).

[94] A. Roshko and G. J. Thomke, "Observations of turbulent reattachment behind an axisymmetric downstream-facing step in supersonic flow." AIAA Journal **4**, 975–980 (1966).

[95] C. F. Coe, "The effects of some variations in launch-vehicle nose shape on steady and fluctuating pressures at transonic speeds," Tech. Rep. TMX-636 (National Aeronautics and Space Administration, 1962).

[96] J. Panda, N. H. Roozeboom, and J. C. Ross, "Wavenumber-Frequency Spectra on a Launch Vehicle Model Measured via Unsteady Pressure-Sensitive Paint," AIAA Journal **57** (2019), 10.2514/1.J057449.

[97] F. Simon, S. Deck, P. Guillen, R. Cayzac, and A. Merlen, "Zonal-Detached-Eddy Simulation of projectiles in the subsonic and transonic regimes," AIAA journal **45**, 1606–1619 (2007).

[98] S. Aksoy and R. M. Haralick, "Feature normalization and likelihood-based similarity measures for image retrieval," Pattern recognition letters **22**, 563–582 (2001).

[99] M. Shanker, M. Y. Hu, and M. S. Hung, "Effect of Data Standardization on Neural Network Training," Omega **24**, 385–397 (1996).

[100] G. Varoquaux, L. Buitinck, G. Louppe, O. Grisel, F. Pedregosa, and A. Mueller, "Scikit-learn," Journal of Machine Learning Research **12**, 2825–2830 (2011).

[101] A. Agarwal, P. Barham, E. Brevdo, Z. Chen, C. Citro, G. S. Corrado, A. Davis, J. Dean, M. Devin, S. Ghemawat, I. Goodfellow, A. Harp, G. Irving, M. Isard, Y. Jia, R. Jozefowicz, L. Kaiser, M. Kudlur, J. Levenberg, D. Man, R. Monga, S. Moore, D. Murray, C. Olah, M. Schuster, J. Shlens, B. Steiner, I. Sutskever, K. Talwar, P. Tucker, V. Vanhoucke, V. Vasudevan, F. Vi, O. Vinyals, P. Warden, M. Wattenberg, M. Wicke, Y. Yu, and X. Zheng, "TensorFlow: Large-Scale Machine Learning on Heterogeneous Distributed Systems," (2015), arXiv:1603.04467v2.

[102] F. Chollet, "Keras," https://keras.io (2015).

[103] A. Fischer, F. Bertagnolio, and H. A. Madsen, "Improvement of TNO type trailing edge noise models," European Journal of Mechanics, B/Fluids **61**, 255–262 (2017).

[104] S. Ye, Z. Zhang, X. Song, Y. Wang, Y. Chen, and C. Huang, "A flow feature detection method for modeling pressure distribution around a cylinder in non-uniform flows by using a convolu-

Accepted to Phys. Fluids 10.1063/5.0146358

tional neural network," Scientific Reports **10**, 1–10 (2020).

[105] B. Liu, J. Tang, H. Huang, and X.-Y. Lu, "Deep learning methods for super-resolution reconstruction of turbulent flows," Physics of Fluids **32**, 025105 (2020).

[106] T. Nakamura, K. Fukami, K. Hasegawa, Y. Nabae, and K. Fukagata, "Convolutional neural network and long short-term memory based reduced order surrogate for minimal turbulent channel flow," Physics of Fluids **33**, 025116 (2021).

[107] D. P. Kingma and J. L. Ba, "Adam: A method for stochastic optimization," 3rd International Conference on Learning Representations, ICLR 2015 - Conference Track Proceedings , 1–15 (2015), arXiv:1412.6980.

[108] I. Goodfellow, Y. Bengio, and A. Courville, "Deep learning," Genetic Programming and Evolvable Machines **19**, 305–307 (2018).

[109] S. Lee and D. You, "Analysis of a convolutional neural network for predicting unsteady volume wake flow fields," Physics of Fluids **33** (2021).

[110] J. Panda, T. J. Garbeff, N. J. Burnside, and J. C. Ross, "Unsteady pressure fluctuations measured on a hammerhead space vehicle and comparison with Coe and Nute's 1962 data," International Journal of Aeroacoustics **17**, 70–87 (2018).